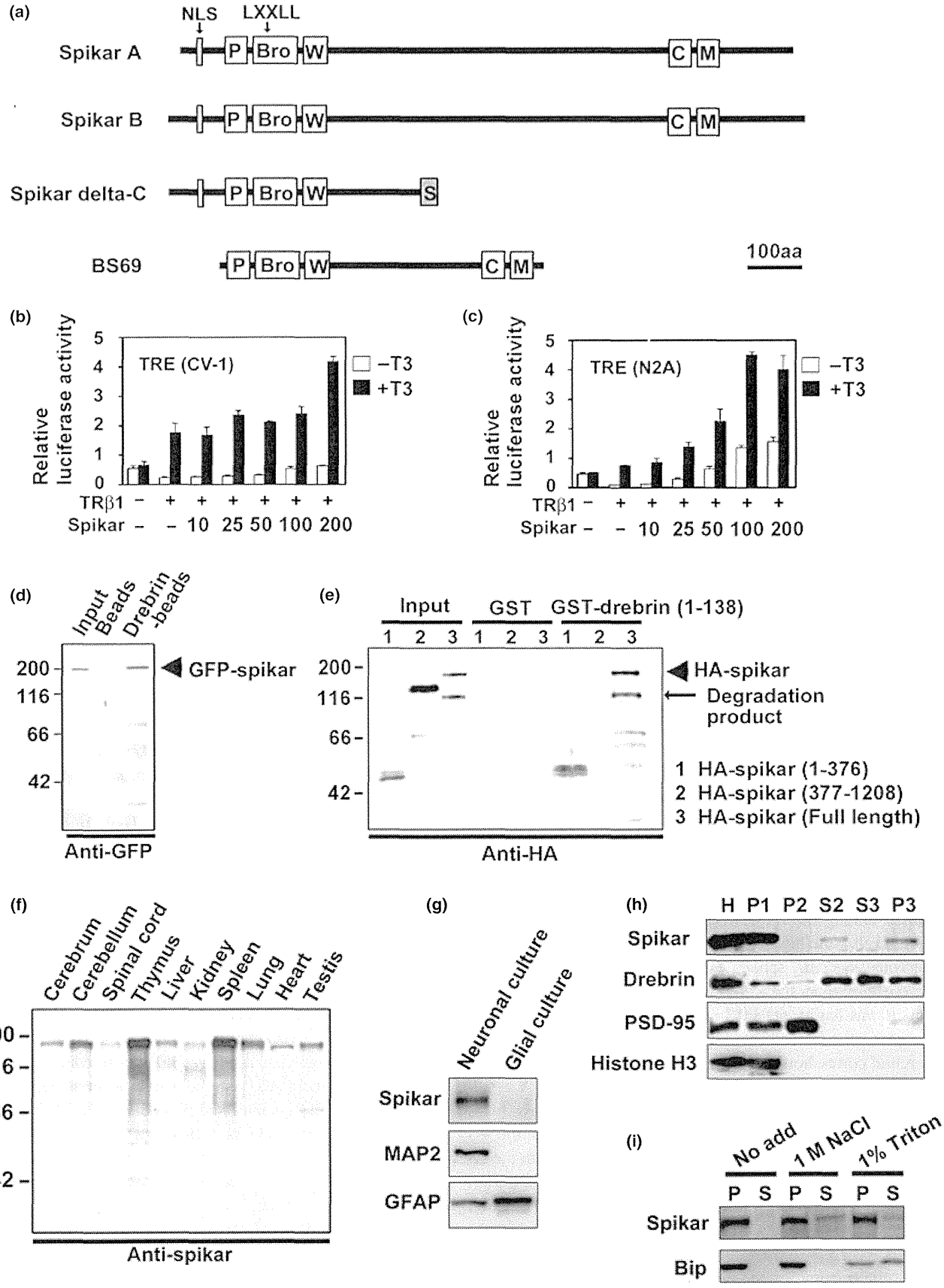
(a)
NLS
LXXLL
Spikar A
Spikar B
Spikar delta-C
BS69
P
Bro
W
C
M
S
100aa
(b)
Relative luciferase activity
TRE (CV-1)
−T3
+T3
TRβ1 − + + + + + +
Spikar − − 10 25 50 100 200
(c)
Relative luciferase activity
TRE (N2A)
−T3
+T3
TRβ1 − + + + + + +
Spikar − − 10 25 50 100 200
(d)
Input
Beads
Drebrin -beads
200
116
66
42
GFP-spikar
Anti-GFP
(e)
Input
GST
GST-drebrin (1-138)
1 2 3 1 2 3 1 2 3
200
116
66
42
HA-spikar
Degradation product
1 HA-spikar (1-376)
2 HA-spikar (377-1208)
3 HA-spikar (Full length)
Anti-HA
(f)
Cerebrum
Cerebellum
Spinal cord
Thymus
Liver
Kidney
Spleen
Lung
Heart
Testis
200
116
66
42
Anti-spikar
(g)
Neuronal culture
Glial culture
Spikar
MAP2
GFAP
(h)
H P1 P2 S2 S3 P3
Spikar
Drebrin
PSD-95
Histone H3
(i)
No add
1 M NaCl
1% Triton
P S P S P S
Spikar
Bip

Fig. 1 Characterization of spikar. (a) Schematic diagram of domain structures of spikar isoforms and BS69. P, Plant Homeo Domain (PHD) domain; Bro, Bromo domain; W, PWWP domain; C, Coiled-coil; M, MYND domain. (b, c) Spikar-activated nuclear-receptor-mediated transcription in CV-1 (b) and N2A cells (c). Cells were grown in the presence or absence of T3 (100 nM). (d) *In vitro* binding assay for the interaction between drebrin and spikar. Input: cell lysate containing GFP-spikar; Beads: samples precipitated with Ni-NTA beads; Drebrin-beads: samples precipitated with drebrin-conjugated beads. (e) GST pull-down assay for spikar and drebrin. Lysates of cells expressing each HA-spikar fragment (1, 1–376; 2, 377–1208; 3, 1–1208) were pulled down with GST-drebrin (1–134). (f) Western blotting of extracts from various tissues (200 μg wet weight for each). (g) Western blotting of lysates (5 μg protein) from neural and glial cultures. (h) Subcellular distribution of spikar. The protein extract (20 μg protein) from each fraction was analyzed by western blotting. H, homogenate; P1, cell nuclei and debris; P2, synaptosomal fraction; S2, non-synaptosomal fraction; S3, cytosolic fraction; P3, microsomal fraction. (i) The P3 fraction from rat cerebral cortices was treated with 1 M NaCl or 1% Triton X-100. The insoluble pellet (P) and supernatant (S) were analyzed by western blotting.

To assess the specificity of the effect of spikar KD on spine density, we performed a rescue experiment using RNAi-resistant spikar (myc-spikar^R), which is distributed to both the cytoplasm and nucleus (Figure S7a), or RNAi-resistant spikar with a mutated nuclear localization sequence (myc-mNLS-spikar^R), which does not enter the nucleus (Figure S7b). Expression of myc-spikar^R significantly increased the density of dendritic spines and filopodia (31.5 ± 1.0 spines/100 μm; 23.2 ± 0.8 filopodia/100 μm; $*p < 0.01$ vs. Spikar KD, Fig. 5e–g) of spikar-KD neurons. Expression of myc-mNLS-spikar^R also rescued the decrease in spine and filopodia densities (30.2 ± 1.1 spines/100 μm; 20.0 ± 0.8 filopodia/100 μm; $*p < 0.01$ vs. Spikar KD, Fig. 5e–g). In addition, we analyzed the dendritic arborization of spikar-KD neurons. Sholl analysis (Sholl 1953) showed that the arborization of the dendrites of spikar-KD neurons was significantly reduced (Figure S8). This phenotype was rescued by cotransfection of myc-mNLS-spikar^R (Figure S8).

Spikar knockdown decreases excitatory synapses

We examined whether spikar KD induces transformation of spine synapses into shaft synapses, or simply the disappearance of spine synapses. Immunocytochemical analysis showed that both PSD-95 and synapsin I clusters were significantly reduced in spikar-KD neurons (Control: PSD-95, 78.1 ± 4.3 clusters/100 μm; synapsin I, 125.4 ± 4.2 clusters/100 μm; Spikar KD: PSD-95, 50.0 ± 2.2 clusters/100 μm; synapsin I, 81.1 ± 2.9 clusters/100 μm; $*p < 0.01$, Fig. 4a and b). Synaptic PSD-95 clusters that were co-localized with synapsin I clusters were also reduced in spikar-KD neurons (Control, 63.0 ± 4.2 clusters/100 μm; Spikar KD, 34.0 ± 1.9 clusters/100 μm; $*p < 0.01$, Fig. 4b, right).

We next analyzed the spontaneous synaptic activity of spikar-KD neurons using electrophysiology (Fig. 4c). The amplitude of mEPSCs in spikar-KD neurons was 20.1 ± 2.0 pA, which was similar to that observed in control neurons (19.1 ± 2.3 pA; Fig. 4d). However, the inter-event interval of mEPSCs was significantly longer in spikar-KD neurons than in control neurons (568.8 ± 98.8 ms and 320.7 ± 63.5 ms, respectively, $p < 0.05$; Fig. 4e). These immunohistochemical and electrophysiological data indicate that spikar KD decreases the density of excitatory synapses, and suggest that spikar regulates the dendritic spine density with a concomitant change in the density of excitatory synapses.

Spikar knockdown facilitates the retraction of existing spines and suppresses the addition of new spines

To analyze whether spikar functions in spine stabilization or *de novo* spine formation, we followed the fate of spines using live-cell imaging (Fig. 5a). Cultured hippocampal neurons were transfected at 8 DIV with spikar-KD vector, and the same cells were analyzed at 16 and 22 DIV (a mature stage of cultured neurons) by imaging GFP fluorescence (Fig. 5b). During the 6-day period from 16 to 22 DIV, the number of retracted spines significantly increased (Control, 9.1 ± 1.0 spines/100 μm; Spikar KD, 15.5 ± 1.3; $*p < 0.01$), and the numbers of persistent and additional spines were significantly decreased (Control: persistent, 15.3 ± 0.9 spines/100 μm; addition, 20.5 ± 2.1; Spikar KD: persistent, 6.2 ± 1.6; addition, 4.2 ± 0.7; $*P < 0.01$) in spikar-KD neurons (Fig. 5c). These effects of spikar KD were blocked by the co-expression of myc-mNLS-spikar^R (retraction, 7.8 ± 0.7 spines/100 μm; persistent, 15.2 ± 1.2; addition, 18.9 ± 1.4; $*P < 0.01$ vs. Spikar KD, Fig. 5c). These results indicate that extranuclear spikar is required for the *de novo* formation and stabilization of dendritic spines.

Localization of spikar in dendritic spines depends on drebrin

To test whether the subcellular localization of spikar depends on drebrin, we performed a transfection study using HEK293 cells. When the cells were transfected with GFP-spikar, the GFP signal was localized to the nucleus and rarely observed in the cytoplasm (Fig. 6a). In contrast, when the cells were co-transfected with GFP-spikar and monomeric DsRED-drebrin, the percentage of cells in which GFP localized to the cytoplasm in addition to the nucleus was significantly increased (GFP-spikar, 3.2 ± 0.2%; GFP-spikar + monomeric DsRED-drebrin, 22.1 ± 1.5%; $*p < 0.01$, Fig. 6b and c). Therefore, the presence of drebrin facilitated the extranuclear distribution of spikar within the cells, suggesting that drebrin anchors spikar within the cytoplasm. When we

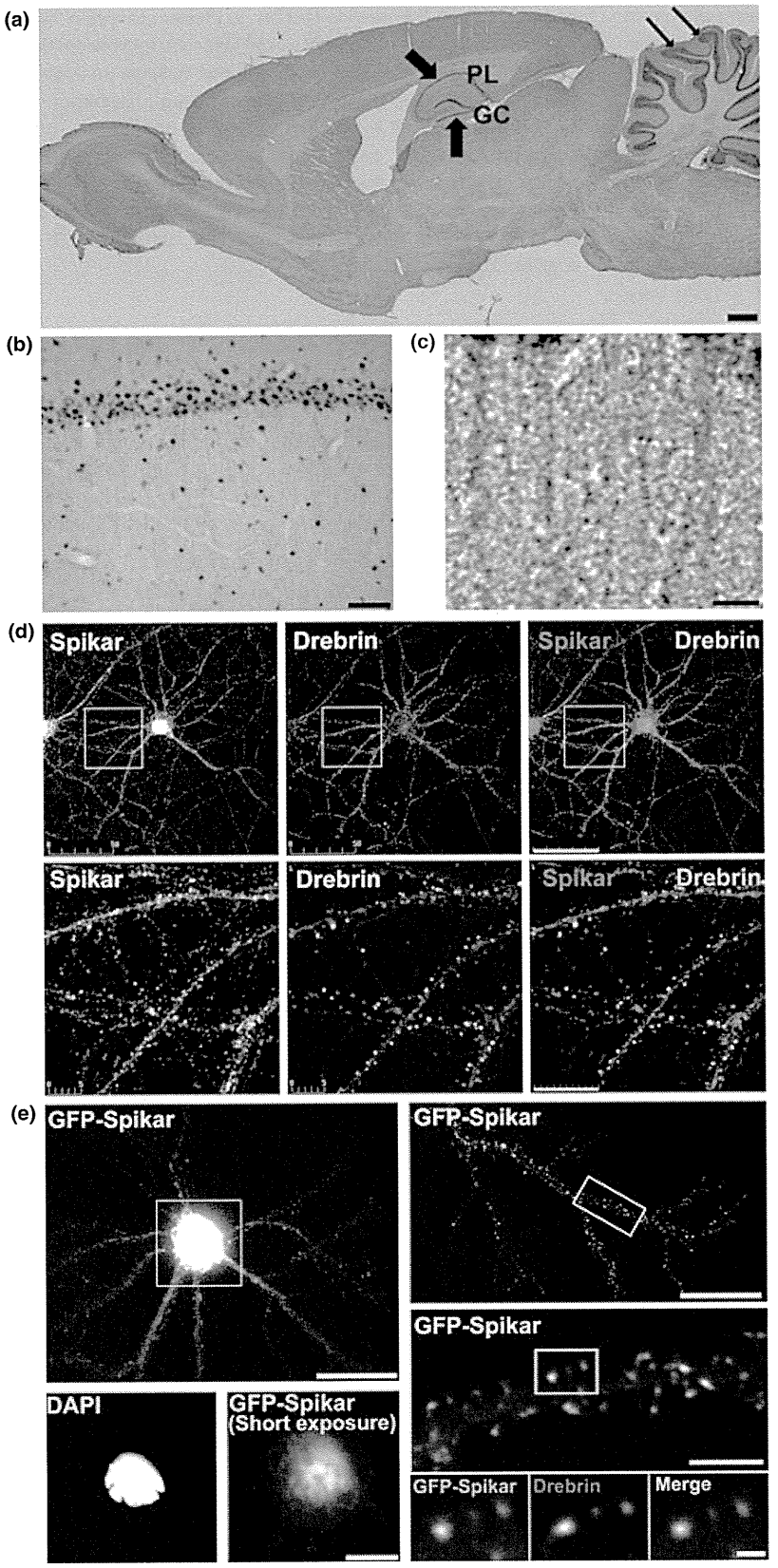

Fig. 2 Spikar is localized in neuronal nuclei and dendritic spines. (a–c) Immunohistochemical staining for spikar in adult rat brain. (a) Low magnification images of sagittal sections. Large arrows indicate granule cell and pyramidal layers of the hippocampus. Small arrows show the granular layer of the cerebellum. Scale bar, 1 mm. (b) Coronal section of hippocampal CA1 region. Scale bar, 50 μm (c) Higher magnification view of pyramidal neurons of the hippocampus. Note the punctate staining pattern observed in the dendritic region. Scale bar, 5 μm. (d) Cultured neurons were immunostained with spikar and drebrin antibodies at 21 DIV. The high magnification views (lower panels) show that spikar signals (red) overlap with drebrin signals (green) in dendritic spines. Scale bars, 50 μm (upper); 10 μm (lower). (e) Cultured neurons were microinjected with GFP-spikar at 21 DIV and analyzed at 22 DIV. Scale bars, 30 μm (upper); 5 μm (lower).

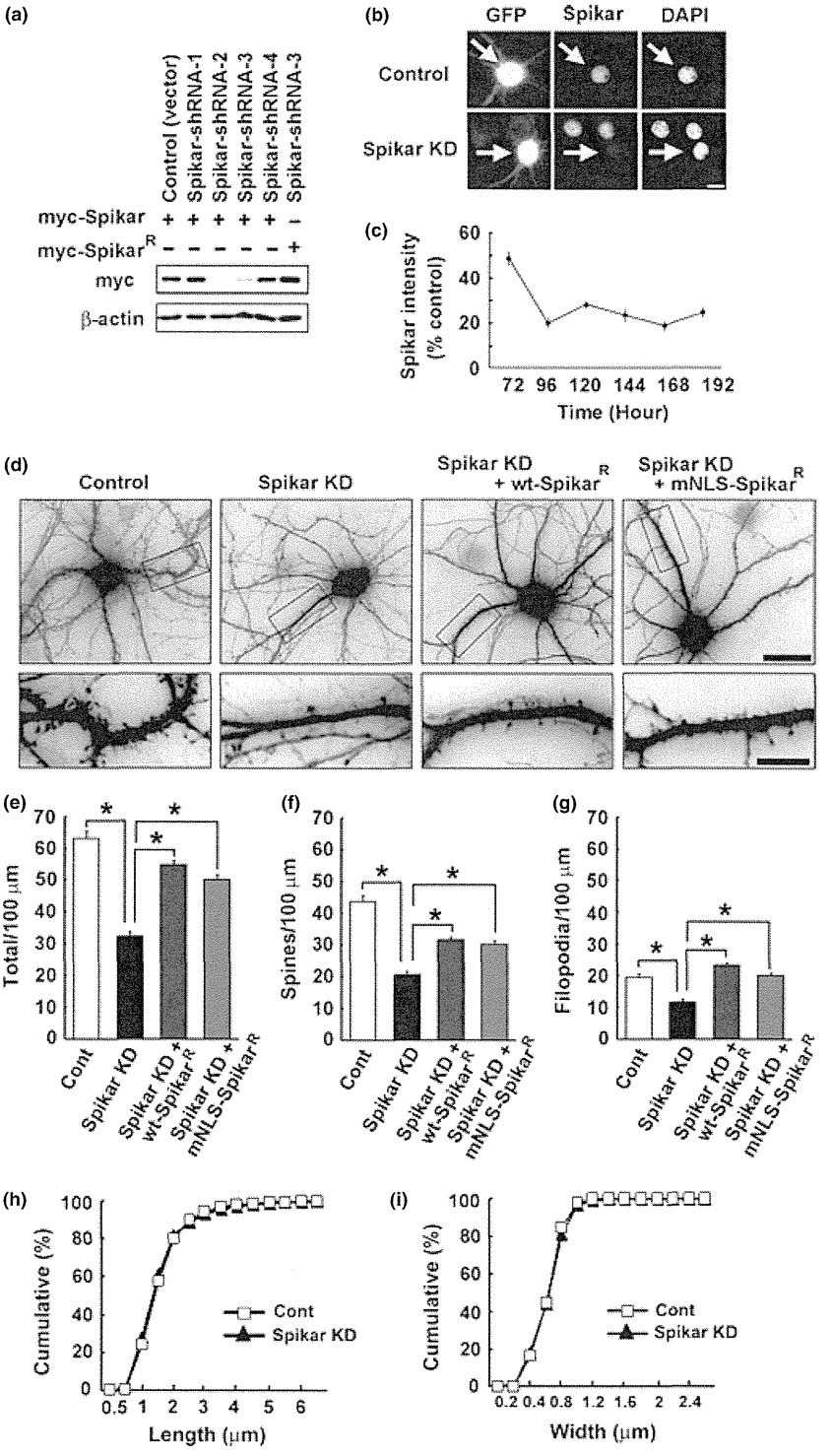

Fig. 3 Spikar knockdown reduces the density of dendritic spines and filopodia. (a) Efficacy of shRNAs. Note that myc-spikar^R is an RNAi-resistant mutant that is not affected by Spikar-shRNA-3. (b) Cultured hippocampal neurons were transfected with either an empty vector (control) or spikar-shRNA-3 and immunostained for spikar. Arrows indicate transfected neurons. Scale bar, 10 μm. (c) Timecourse of spikar knockdown (KD) in cultured hippocampal neurons. (d) Cultured neurons were transfected with an empty vector (cont), spikar-shRNA-3, spikar-shRNA-3+ myc-spikar^R, or spikar-shRNA-3+ myc-mutated nuclear localization sequence (mNLS)-spikar^R at 3 DIV and analyzed at 16 DIV. Scale bars, 30 μm (upper) and 10 μm (lower). (e–g) Quantification of effects of spikar KD on the density of total protrusions (spines and filopodia), spines, and filopodia. Data are presented as mean ± SEM ($n > 100$, $^*p < 0.01$, Tukey–Kramer test). (h, i) Cumulative frequency plots of the length and width of dendritic protrusions in neurons transfected with empty vector or spikar-shRNA-3. Data were collected from 1800–2500 protrusions from > 100 neurons for each group.

transfected myc-spikar into cultured hippocampal neurons, myc-spikar was localized to dendritic spines and the nucleus, similar to the expression pattern of endogenous spikar (Fig. 6d). In the dendritic spines, strong immunostaining of myc-spikar co-localized with strong drebrin signals. The immunofluorescence intensity of myc-spikar in the dendritic spines correlated with that of drebrin (correlation coefficient $r = 0.59$, $p < 0.01$, Fig. 6e).

Next, we examined whether drebrin KD changed the intracellular localization of myc-spikar in cultured neurons. We silenced the expression of drebrin using RNAi and then analyzed the localization of spikar. Myc-spikar was distrib-

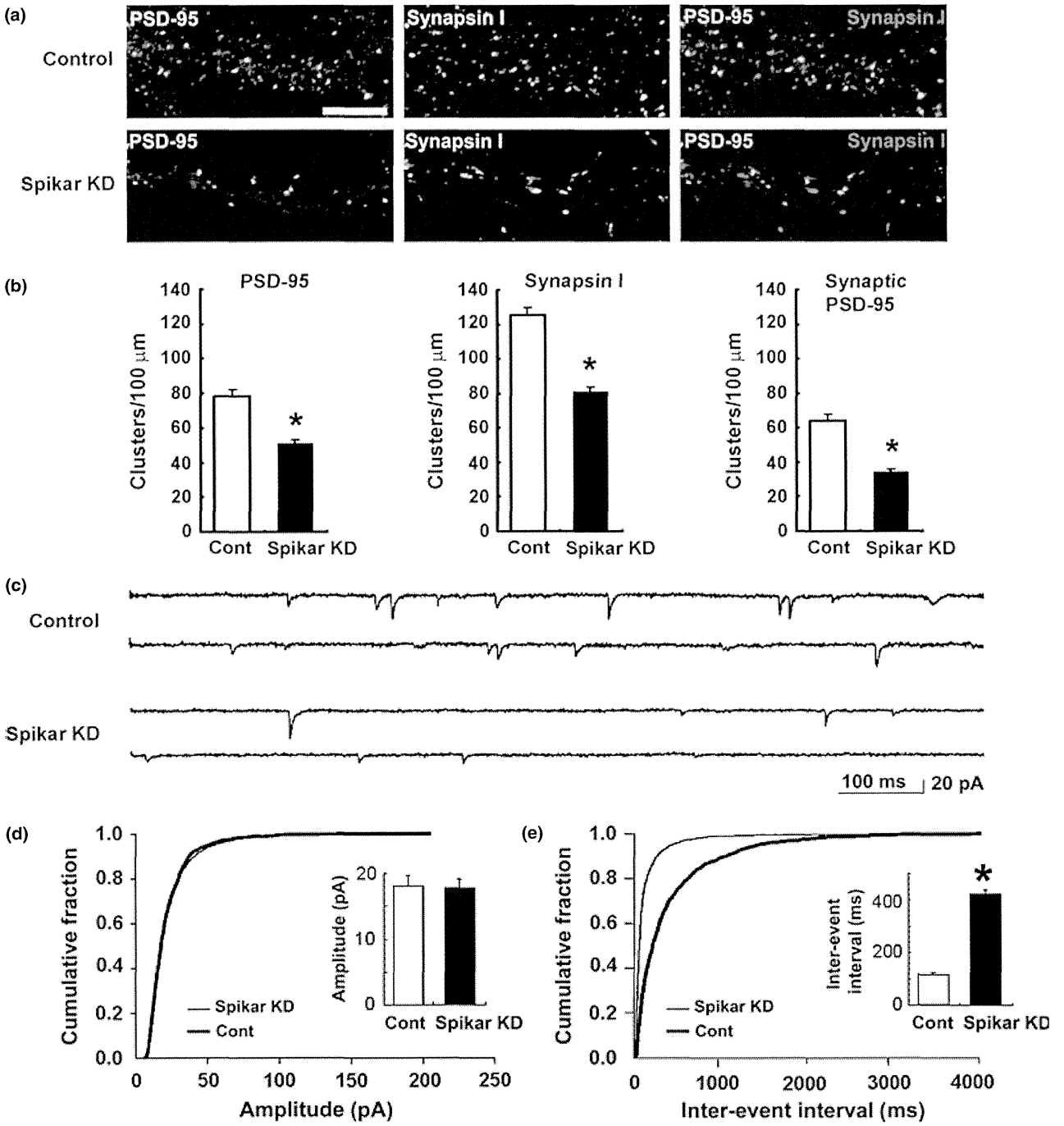

Fig. 4 Knockdown of spikar reduces excitatory synapses. (a) Cultured neurons were transfected with empty vector (cont) or spikar-shRNA-3 at 3 DIV and analyzed at 16 DIV. Spikar-knockdown (KD) neurons were immunolabeled for PSD-95 (green) and Synapsin I (red). Scale bar, 5 μm. (b) Quantification of cluster densities of PSD-95, Synapsin I, and PSD-95/Synapsin I. Data are presented as mean ± SEM (n = 58 and 64 for control and spikar KD, respectively, *p < 0.01, Welch's t-test). Excitatory synapses are defined as synapsin I-positive, PSD-95-positive clusters. (c) Representative recordings of miniature excitatory postsynaptic currents (mEPSCs) from control and spikar-KD neurons. (d, e) Quantification of mEPSC peak amplitudes and mEPSC inter-event intervals from control and spikar-KD neurons. Inset graphs show the mean ± SEM (n = 17 and 16 for control and spikar KD, respectively, *p < 0.01, Welch's t-test).

uted diffusely throughout the dendritic shafts in the drebrin-KD neurons but not in the control neurons (Fig. 6f). To assess the accumulation of spikar in the dendritic spines, the immunofluorescence intensities of myc-spikar were quantified in dendritic spines and shafts, and the ratios of spine to shaft intensities were calculated. The accumulation of myc-

spikar in spines was significantly inhibited by the loss of drebrin (Control spine/shaft intensity, 1.03 ± 0.03; Drebrin KD, 0.61 ± 0.01; $P < 0.01$) and was rescued by co-transfection with an RNAi-resistant drebrin mutant (drebrin^R) (1.86 ± 0.06, $*p < 0.01$ vs. Drebrin KD, Fig. 6g), indicating that the dendritic localization of spikar was dependent on drebrin. However, the C-terminal region of spikar (aa820-1041), which lacks drebrin-binding activity, accumulated in dendritic spines (Figure S9a). Furthermore, the spikar delta-C isoform, which has a drebrin-binding region but lacks the C-terminal region, was not localized in dendritic spines but was solely localized within the nucleus (Figure S9b). Therefore, binding of spikar to drebrin is not always correlated with dendritic spine localization.

Finally, we examined whether spikar affects drebrin localization at dendritic spines (Fig. 6h). In spikar-KD neurons, the percentages of drebrin-positive filopodia and spines in spikar-KD neurons were similar to those in control neurons (Fig. 6i). Furthermore, the drebrin immunofluorescence intensity within drebrin-positive spines was not affected by spikar KD (Fig. 6j). Together, these data indicate that drebrin localization does not depend on spikar, whereas spikar localization does depend on drebrin.

Overexpression of extranuclear spikar facilitates spine formation in a drebrin-dependent manner

To further investigate the function of spikar in the cytoplasm, we performed a spikar gain-of-function experiment by introducing mNLS-spikar into cultured neurons at 8 DIV and measuring the numbers of spines and filopodia at 13 DIV (Fig. 7a). Overexpression of mNLS-spikar significantly increased the densities of both spines and filopodia (Control: 14.9 ± 1.0 spines/100 μm; 33.8 ± 1.5 filopodia/100 μm; mNLS-spikar: 21.9 ± 1.3 spines/100 μm; 46.6 ± 2.0 filopodia/100 μm; $*p < 0.01$, Fig. 7b–d). We then examined whether the spine-formation activity of mNLS-spikar requires the presence of drebrin. We co-transfected mNLS-spikar and drebrin-shRNA into cultured neurons and measured the numbers of spines and filopodia. Drebrin KD (8–13 DIV) abolished the mNLS-spikar-induced increases in spine and filopodia density (Fig. 7b–d). The inhibition of mNLS-spikar function by drebrin KD was

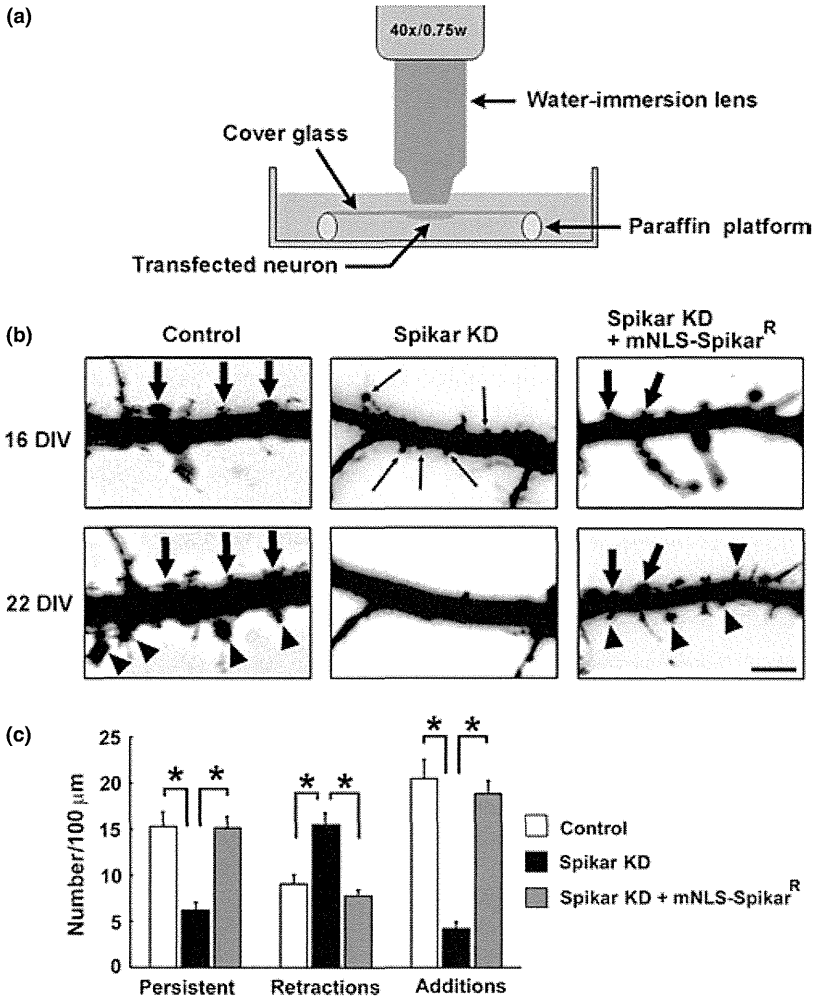

Fig. 5 Live-cell imaging of spikar-knockdown (KD) neurons. (a) Diagram of live-cell imaging method. (b) Cultured neurons were transfected at 8 DIV with empty vector (cont), spikar-shRNA-3, or spikar-shRNA-3+ myc-mutated nuclear localization sequence (mNLS)-spikar^R. Neurons expressing GFP were imaged at 16 and 22 DIV. Arrows indicate spines that were maintained, arrow heads indicate spines that were added, and thin arrows indicate spines that were retracted during the intervening 6-day period. Scale bars, 5 μm. (c) Quantification of the respective fates of spines. Data are presented as mean ± SEM (n = 30, 31, and 47 for control, spikar KD, and spikar KD + myc-mNLS-spikar^R, respectively, $*p < 0.01$, Tukey–Kramer test).

rescued by co-expression of drebrin^{R} (24.0 ± 1.6 spines/100 μm; 46.4 ± 2.8 filopodia/100 μm; *$p < 0.01$ vs. Drebrin KD + mNLS-spikar). Drebrin KD (8–13 DIV) did not affect the densities of spines and filopodia in the control culture (Fig. 7b–d), although prolonged drebrin-KD (3–16 DIV) decreased the density of spines and filopodia (Control: 45.4 ± 2.1 spines/100 μm; 23.5 ± 1.6 filopodia/100 μm; Drebrin KD: 31.6 ± 2.3 spines/100 μm; 17.7 ± 1.3 filopodia/100 μm; *$p < 0.01$, Figure S10a and b). These data indicate that extranuclear spikar facilitates spine formation, and that this effect requires drebrin.

Discussion

In this study, we identified a novel drebrin-binding protein that we named spikar. Spikar was localized in cell nuclei and acted as a transcriptional co-activator. Intriguingly, in neurons, spikar was localized at dendritic spines in addition to cell nuclei. Using a combination of RNAi knockdown and mNLS-spikar overexpression, we have shown that spikar is involved in the regulation of dendritic spine density.

Role of drebrin in subcellular localization of spikar

Because mNLS-spikar, which can bind to drebrin but lacks a normal NLS, is not localized in the nucleus, drebrin does not seem to be involved in the nuclear localization of spikar. However, drebrin overexpression increases the proportion of cytoplasmic spikar within HEK293 cells, and drebrin KD inhibits the dendritic accumulation of spikar. These data indicate that drebrin is involved in the localization of spikar in dendritic spines. The present study also demonstrates that protein–protein interaction plays a role in the recovery of spikar in the microsomal fraction, which contains drebrin. Moreover, the level of myc-spikar in dendritic spines is correlated with that of drebrin. These data suggest that drebrin anchors spikar in dendritic spines.

Our *in vitro* studies reveal that the N-terminal region of spikar binds to the ADF-H domain of drebrin. Although ADF-superfamily proteins generally bind to actin via the ADF-H domain (Lappalainen *et al.* 1998), drebrin binds to F-actin via the central actin-remodeling region (Hayashi *et al.* 1999; Grintsevich *et al.* 2010). Therefore spikar is not likely to compete with the interaction between drebrin and *F*-actin. We suggest that spikar is included in the drebrin-actin complex in dendritic spines via a direct protein–protein interaction between drebrin and spikar.

However, the delta-C isoform of spikar does not localize to dendritic spines despite the presence of a drebrin-binding domain. In addition, a C-terminal region (amino acids 820–1041) of spikar that does not bind to drebrin accumulates in dendritic spines. These data indicate that drebrin binding is not sufficient for spikar to be localized to dendritic spines, and that besides the direct protein–protein interaction between drebrin and spikar, another mechanism involving the C-terminal region of spikar must also play a role in the accumulation of spikar in dendritic spines.

Extranuclear spikar is involved in dendritic spine formation

The present study indicates that expression of either wild-type spikar or mNLS-spikar can rescue the decreased spine density of spikar-KD neurons. In addition, overexpression of mNLS-spikar increases the spine density of normal cells. Furthermore, our time-lapse imaging data indicate that mNLS-spikar increases the *de novo* formation of spines and decreases the retraction of existing spines in spikar-KD neurons. Because these data indicate that the expression level of extranuclear spikar relates directly to spine density, changes in transcription of other genes, which are likely to be induced by spikar, are not necessary for spine formation. However, we do not deny a possibility of involvement of spikar-mediated transcription in spine formation outright because mNLS-spikar did not rescue the spine density completely. Furthermore, the inhibitory effect of spikar-KD on dendritic branching might affect the formation of spines.

When spine density is decreased by spikar KD, the remaining spines show normal morphologies. In addition, although the frequency of AMPAR-mediated mEPSCs is decreased following spikar KD, the amplitude is not affected. Thus, it is suggested that spikar is involved in the formation

Fig. 6 Drebrin mediates spikar anchoring at dendritic spines. (a) HEK293 cells were transfected with GFP-spikar or GFP-spikar + mDsRED-drebrin. Cytoplasmic GFP-spikar was selectively imaged by subtracting the DAPI signal from GFP images (Subtraction). Scale bar, 50 μm. (b) High magnification image of a co-transfected cell. Scale bar, 20 μm. (c) The ratio of cells possessing cytoplasmic spikar to the total number of transfected cells was significantly increased in the presence of drebrin ($n = 30$ fields, *$p < 0.01$, Mann–Whitney U-test). (d) Cultured neurons were transfected with myc-spikar, and immunostained with myc-spikar (red) and drebrin (green). Scale bars, 30 μm (upper) and 5 μm (lower). (e) Immunofluorescence intensities of myc-spikar and drebrin in spines were significantly correlated ($r = 0.59$, $p < 0.01$). (f) Cultured hippocampal neurons were transfected at 8 DIV with empty vector (cont), or drebrin-shRNA + myc-spikar, or drebrin-shRNA + myc-spikar + HA-drebrin^{R}. Scale bar, 5 μm. (g) Quantification of the effect of drebrin knockdown (KD) on spine localization of myc-spikar. Data are presented as mean ± SEM ($n > 400$ spines from 30 neurons, *$p < 0.01$, Steel–Dwass test). (h) Cultured neurons were transfected with empty vector (control) or spikar-shRNA-3 (3–16 DIV). Transfected neurons were immunolabeled with antibody for drebrin. Scale bar, 5 μm. (i, j) Quantification of effects of spikar KD on the percentage of drebrin-positive protrusions (i) and the immunofluorescence intensity of drebrin (j). Data are presented as mean ± SEM ($n = 50$ for each group).

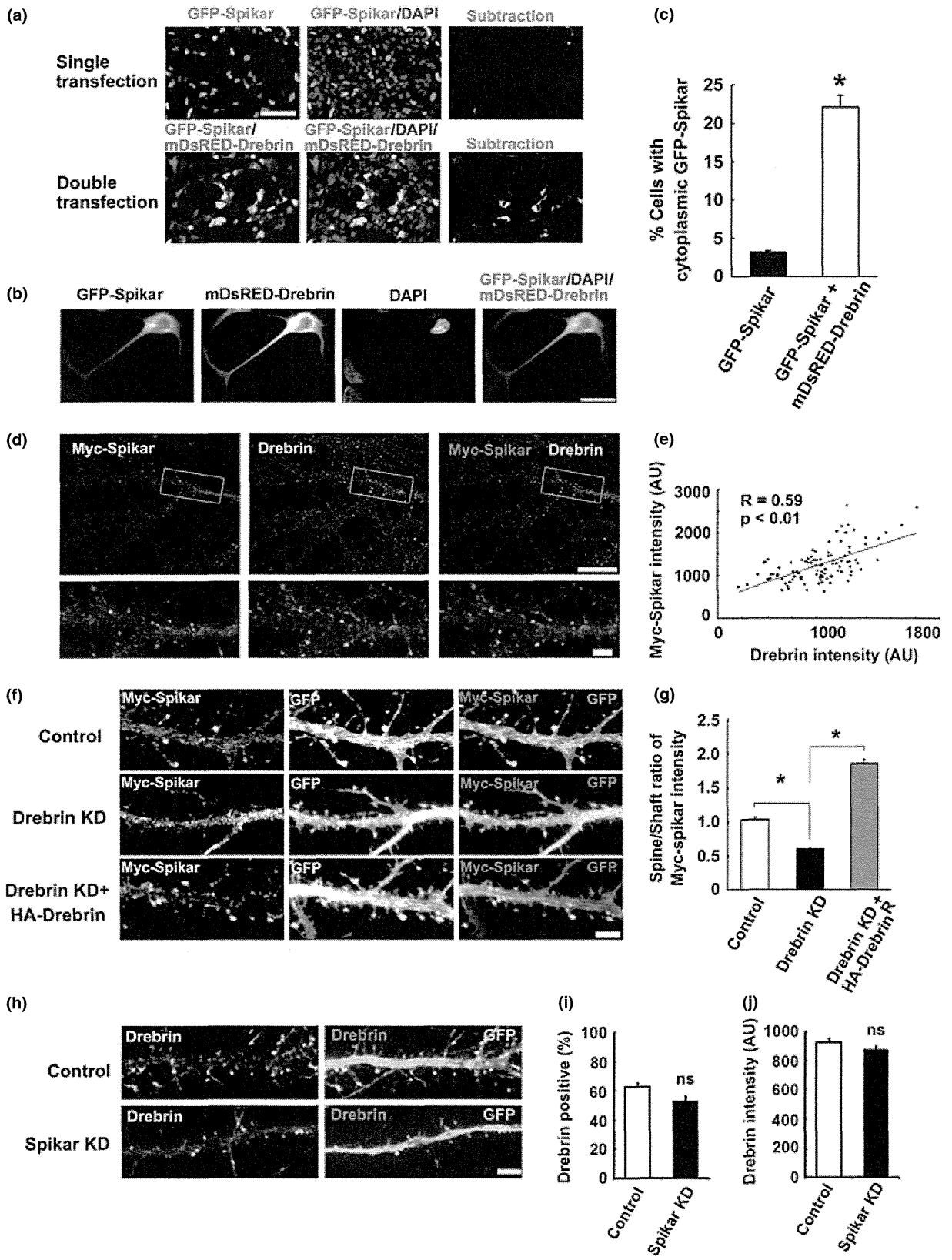
(a)
GFP-Spikar
GFP-Spikar/DAPI
Subtraction
Single transfection
GFP-Spikar/ mDsRED-Drebrin
GFP-Spikar/DAPI/ mDsRED-Drebrin
Subtraction
Double transfection
(b)
GFP-Spikar
mDsRED-Drebrin
DAPI
GFP-Spikar/DAPI/ mDsRED-Drebrin
(c)
% Cells with cytoplasmic GFP-Spikar
25
20
15
10
5
0
*
GFP-Spikar
GFP-Spikar + mDsRED-Drebrin
(d)
Myc-Spikar
Drebrin
Myc-Spikar Drebrin
(e)
Myc-Spikar intensity (AU)
3000
2000
1000
0
R = 0.59
p < 0.01
0
1000
1800
Drebrin intensity (AU)
(f)
Control
Drebrin KD
Drebrin KD+ HA-Drebrin
Myc-Spikar
GFP
(g)
Spine/Shaft ratio of Myc-spikar intensity
2.5
2.0
1.5
1.0
0.5
0
*
*
Control
Drebrin KD
Drebrin KD+ HA-Drebrin R
(h)
Control
Spikar KD
Drebrin
GFP
(i)
Drebrin positive (%)
100
80
60
40
20
0
ns
Control
Spikar KD
(j)
Drebrin intensity (AU)
1000
800
600
400
200
0
ns
Control
Spikar KD

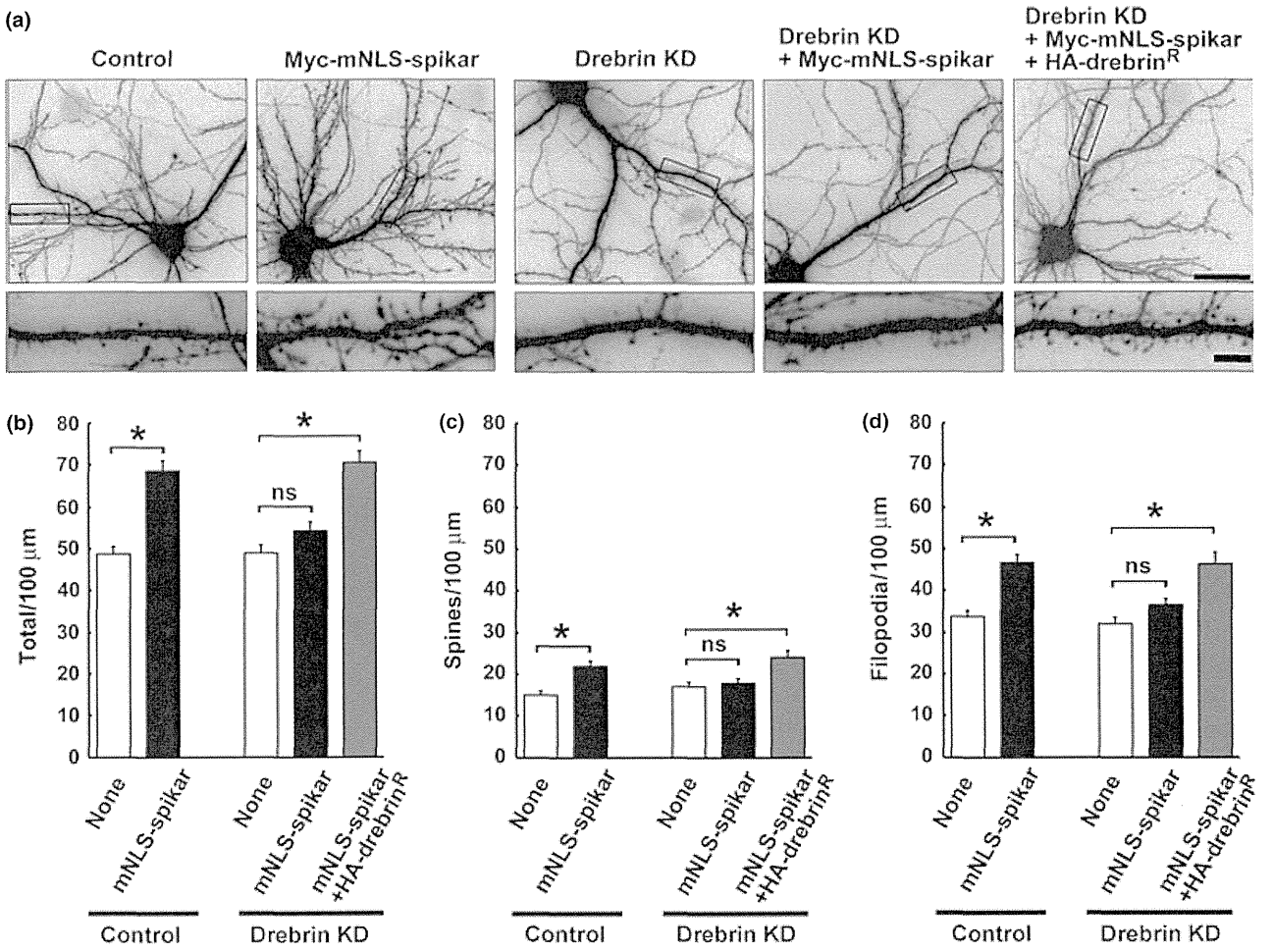

Fig. 7 Effect of extranuclear spikar overexpression is inhibited by drebrin knockdown (KD). (a) Cultured neurons were transfected after 8 DIV with empty vector (control), empty vector + myc-mutated nuclear localization sequence (mNLS)-Spikar, drebrin-shRNA, drebrin-shRNA + myc-mNLS-Spikar, or drebrin-shRNA + myc-mNLS-Spikar + HA-drebrin^R. GFP images were analyzed at 13 DIV. Scale bars, 30 μm (upper); 5 μm (lower). (b–d) Quantification of spine and filopodia density for each experimental condition. Data are presented as mean ± SEM ($n = 55$ for each group, $^*p < 0.01$, Tukey–Kramer test).

and stabilization of dendritic spines, but it is not involved in the function of mature spines.

Role of drebrin–spikar interaction in spine formation

Interestingly, overexpression of mNLS-spikar did not increase spine density in drebrin-KD neurons. This suggests that drebrin-mediated anchoring of spikar through protein-protein interaction at dendritic spines is necessary for increasing spine density. An alternative explanation is that the decrease in spine density caused by drebrin KD counteracts the increase induced by spikar overexpression. We and others have previously shown that drebrin KD inhibits spine formation (Takahashi *et al.* 2006; Biou *et al.* 2008). In fact, we detected a significant decrease in spine density in longer duration (3–16 DIV) drebrin KD. Therefore, spikar might function in a different regulatory pathway from drebrin. However, we did not detect any decrease in spine density in a drebrin-KD experiment of the same duration (8–13 DIV) as the mNLS-spikar overexpression experiment. This result indicates that the likelihood of the latter possibility is low, although it is not known why shorter term drebrin KD (8–13 DIV) did not lead to a decrease in spine density similar to prolonged drebrin KD (3–16 DIV). The reduction of drebrin expression in drebrin KD (8–13 DIV) neurons might be sufficient to block *de novo* spine formation induced by overexpressed mNLS-spikar, but not enough to decrease the spine density compared with the reduction in drebrin KD (3–16 DIV).

While the present study indicates that spikar KD does not affect spine morphology, our previous study demonstrated that drebrin KD does alter spine morphology (Takahashi *et al.* 2006). It has been reported that drebrin accumulates at nascent excitatory postsynaptic sites (Aoki *et al.* 2005) before the accumulation of PSD-95 (Takahashi *et al.* 2003)

and drebrin is suggested to play a pivotal role in forming a unique stable actin structure at postsynaptic sites (Shirao and Gonzalez-Billault 2013). Spikar may be recruited to the actin structure by binding to drebrin, and consequently functions in the spikar-mediated spine density regulatory pathway. In this context, other proteins recruited to the stable actin structure could mediate the morphological changes in dendritic spines, in a manner distinct from the spikar-mediated regulatory pathway.

Several molecules have been reported to be involved in dendritic spine formation and stabilization (McMahon and Diaz 2011). Diacylglycerol kinase (DGK)ζ is a DGK isoform that is enriched at excitatory synapses. DGKζ KD is known to reduce spine stability and density without changing spine morphology (Kim *et al.* 2009). Furthermore, the loss of DGKζ decreases the frequency of mEPSCs without affecting their amplitudes (Kim *et al.* 2009). Because these morphological and electrophysiological phenotypes of DGKζ KD are similar to those of spikar KD, it is suggested that spikar and DGKζ might be involved in a similar pathway regulating dendritic spine formation and stabilization, although an interaction between DGKζ and drebrin has not been reported.

Some cell adhesion molecules are also involved in dendritic spine formation and stabilization. Knockdown of N-cadherin reduces the stability of dendritic spines (Mendez *et al.* 2010), and a dominant-negative disruption of leukocyte common antigen-related (LAR) receptor protein tyrosine phosphatase function increases the retraction of existing spines and decreases *de novo* spine formation (Dunah *et al.* 2005). Although these phenotypes are similar to those of spikar KD, unlike spikar KD, the functional inhibition of N-cadherin or LAR results in formation of smaller dendritic spines. Therefore, spikar is likely to be involved in a different regulatory pathway from N-cadherin or LAR.

Acknowledgments

We thank Dr Ryoki Ishikawa for His6-drebrin. T7 work was supported by Grants-in-Aid for Young Scientists (15700285, 18700306, 21700340) and a Grant-in-Aid for Scientific Research (19200029) from the Japan Society for the Promotion of Science (JSPS). All authors declare that they have no conflict of interest.

Supporting information

Additional supporting information may be found in the online version of this article at the publisher's web-site:

Appendix S1. The expression vectors for TRβ1 and ERα (Takeshita *et al.* 1998), and GR (Iwasaki *et al.* 2001) have been described previously.

Figure S1. (a) The spikar antibody recognized GFP-spikar as a single band at approximately 200 kDa, demonstrating that the spikar antibody specifically recognized spikar protein.

Figure S2. (a) Cultured neurons were transfected with an empty vector (control), luciferase-shRNA, or spikar-shRNA-2 at 3 DIV, and analyzed at 16 DIV.

Figure S3. (a) Higher magnification image of dendritic spines. The neuron is transfected with GFP. Scale bar, 2 μm. (b) Illustration of panel (a).

Figure S4. (a, b) Spikar activated transcription mediated by the glucocorticoid receptor (GR) and estrogen receptor α (ERα) in CV-1 cells.

Figure S5. (e, f) Interaction between drebrin and spikar were assayed by HIS3 induction in the yeast two-hybrid system.

Figure S6. (a, b) Immunofluorescence localization of spikar in cultured GFP-transfected neurons at two developmental stages (7 DIV and 14 DIV).

Figure S7. (a, b) Cultured hippocampal neurons were transfected at 8 DIV with myc-spikar (a) or myc-mNLS-spikar (b), and immunostained with anti-myc antibody at 16 DIV.

Figure S8. Cultured neurons were transfected with an empty vector (cont), spikar-shRNA-3, spikar-shRNA-3 + myc-spikarR, or spikar-shRNA-3 + myc-mNLS-spikarR at 3 DIV and analyzed at 16 DIV.

Figure S9. (a) Cultured neurons were transfected with GFP-spikar (820-1041) at 8 DIV and analyzed at 16 DIV. GFP-spikar (820-1041), which does not bind to drebrin, was localized in dendritic spines. Scale bar, 5 μm.

Figure S10. (a) Cultured neurons were transfected with empty vector (control) or drebrin-shRNA at 3 DIV and analyzed at 16 DIV. Prolonged drebrin KD decreased the density of dendritic spines and filopodia. Scale bars, 30 μm (upper); 5 μm (lower).

References

Aoki C., Sekino Y., Hanamura K., Fujisawa S., Mahadomrongkul V., Ren Y. and Shirao T. (2005) Drebrin A is a postsynaptic protein that localizes in vivo to the submembranous surface of dendritic sites forming excitatory synapses. *J. Comp. Neurol.* **483**, 383–402.

Biou V., Brinkhaus H., Malenka R. C. and Matus A. (2008) Interactions between drebrin and Ras regulate dendritic spine plasticity. *Eur. J. Neurosci.* **27**, 2847–2859.

Dotti C. G., Sullivan C. A. and Banker G. A. (1988) The establishment of polarity by hippocampal neurons in culture. *J. Neurosci.* **8**, 1454–1468.

Dunah A. W., Hueske E., Wyszynski M., Hoogenraad C. C., Jaworski J., Pak D. T., Simonetta A., Liu G. and Sheng M. (2005) LAR receptor protein tyrosine phosphatases in the development and maintenance of excitatory synapses. *Nat. Neurosci.* **8**, 458–467.

Ethell I. M. and Pasquale E. B. (2005) Molecular mechanisms of dendritic spine development and remodeling. *Prog. Neurobiol.* **75**, 161–205.

Fossey S. C., Kuroda S., Price J. A., Pendleton J. K., Freedman B. I. and Bowden D. W. (2000) Identification and characterization of PRKCBP1, a candidate RACK-like protein. *Mamm. Genome* **11**, 919–925.

Gorlich A., Zimmermann A. M., Schober D., Bottcher R. T., Sassoe-Pognetto M., Friauf E., Witke W. and Rust M. B. (2012) Preserved morphology and physiology of excitatory synapses in profilin1-deficient mice. *PLoS ONE* **7**, e30068.

Grintsevich E. E., Galkin V. E., Orlova A., Ytterberg A. J., Mikati M. M., Kudryashov D. S., Loo J. A., Egelman E. H. and Reisler E. (2010) Mapping of drebrin binding site on F-actin. *J. Mol. Biol.* **398**, 542–554.

Hayashi K. and Shirao T. (1999) Change in the shape of dendritic spines caused by overexpression of drebrin in cultured cortical neurons. *J. Neurosci.* **19**, 3918–3925.

Hayashi K., Ishikawa R., Ye L. H., He X. L., Takata K., Kohama K. and Shirao T. (1996) Modulatory role of drebrin on the cytoskeleton within dendritic spines in the rat cerebral cortex. *J. Neurosci.* **16**, 7161–7170.

Hayashi K., Ishikawa R., Kawai-Hirai R., Takagi T., Taketomi A. and Shirao T. (1999) Domain analysis of the actin-binding and actin-remodeling activities of drebrin. *Exp. Cell Res.* **253**, 673–680.

Huttner W. B., Schiebler W., Greengard P. and De Camilli P. (1983) Synapsin I (protein I), a nerve terminal-specific phosphoprotein. III. Its association with synaptic vesicles studied in a highly purified synaptic vesicle preparation. *J. Cell Biol.* **96**, 1374–1388.

Ishikawa R., Hayashi K., Shirao T., Xue Y., Takagi T., Sasaki Y. and Kohama K. (1994) Drebrin, a development-associated brain protein from rat embryo, causes the dissociation of tropomyosin from actin filaments. *J. Biol. Chem.* **269**, 29928–29933.

Ishikawa R., Katoh K., Takahashi A., Xie C., Oseki K., Watanabe M., Igarashi M., Nakamura A. and Kohama K. (2007) Drebrin attenuates the interaction between actin and myosin-V. *Biochem. Biophys. Res. Commun.* **359**, 398–401.

Ivanov A., Esclapez M., Pellegrino C., Shirao T. and Ferhat L. (2009) Drebrin A regulates dendritic spine plasticity and synaptic function in mature cultured hippocampal neurons. *J. Cell Sci.* **122**, 524–534.

Iwasaki T., Chin W. W. and Ko L. (2001) Identification and characterization of RRM-containing coactivator activator (CoAA) as TRBP-interacting protein, and its splice variant as a coactivator modulator (CoAM). *J. Biol. Chem.* **276**, 33375–33383.

Iwasaki T., Miyazaki W., Takeshita A., Kuroda Y. and Koibuchi N. (2002) Polychlorinated biphenyls suppress thyroid hormone-induced transactivation. *Biochem. Biophys. Res. Commun.* **299**, 384–388.

Kato K., Shirao T., Yamazaki H., Imamura K. and Sekino Y. (2012) Regulation of AMPA receptor recruitment by the actin binding protein drebrin in cultured hippocampal neurons. *JNSNE* **1**, 153–160.

Kim K., Yang J., Zhong X. P. *et al.* (2009) Synaptic removal of diacylglycerol by DGKzeta and PSD-95 regulates dendritic spine maintenance. *EMBO J.* **28**, 1170–1179.

Kojima N., Wang J., Mansuy I. M., Grant S. G., Mayford M. and Kandel E. R. (1997) Rescuing impairment of long-term potentiation in fyn-deficient mice by introducing Fyn transgene. *Proc. Natl Acad. Sci. USA* **94**, 4761–4765.

Kwon H. B. and Sabatini B. L. (2011) Glutamate induces de novo growth of functional spines in developing cortex. *Nature* **474**, 100–104.

Lappalainen P., Kessels M. M., Cope M. J. and Drubin D. G. (1998) The ADF homology (ADF-H) domain: a highly exploited actin-binding module. *Mol. Biol. Cell* **9**, 1951–1959.

Mammoto A., Sasaki T., Asakura T., Hotta I., Imamura H., Takahashi K., Matsuura Y., Shirao T. and Takai Y. (1998) Interactions of drebrin and gephyrin with profilin. *Biochem. Biophys. Res. Commun.* **243**, 86–89.

Masselink H. and Bernards R. (2000) The adenovirus E1A binding protein BS69 is a corepressor of transcription through recruitment of N-CoR. *Oncogene* **19**, 1538–1546.

McMahon S. A. and Diaz E. (2011) Mechanisms of excitatory synapse maturation by trans-synaptic organizing complexes. *Curr. Opin. Neurobiol.* **21**, 221–227.

Mendez P., De Roo M., Poglia L., Klauser P. and Muller D. (2010) N-cadherin mediates plasticity-induced long-term spine stabilization. *J. Cell Biol.* **189**, 589–600.

Mizui T., Takahashi H., Sekino Y. and Shirao T. (2005) Overexpression of drebrin A in immature neurons induces the accumulation of F-actin and PSD-95 into dendritic filopodia, and the formation of large abnormal protrusions. *Mol. Cell. Neurosci.* **30**, 630–638.

Rochefort N. L. and Konnerth A. (2012) Dendritic spines: from structure to in vivo function. *EMBO Rep.* **13**, 699–708.

Ryu J., Liu L., Wong T. P., Wu D. C., Burette A., Weinberg R., Wang Y. T. and Sheng M. (2006) A critical role for myosin IIb in dendritic spine morphology and synaptic function. *Neuron* **49**, 175–182.

Sala C., Futai K., Yamamoto K., Worley P. F., Hayashi Y. and Sheng M. (2003) Inhibition of dendritic spine morphogenesis and synaptic transmission by activity-inducible protein Homer1a. *J. Neurosci.* **23**, 6327–6337.

Sala C., Cambianica I. and Rossi F. (2008) Molecular mechanisms of dendritic spine development and maintenance. *Acta. Neurobiol. Exp.* **68**, 289–304.

Sekiguchi T., Hirose E., Nakashima N., Ii M. and Nishimoto T. (2001) Novel G proteins, Rag C and Rag D, interact with GTP-binding proteins, Rag A and Rag B. *J. Biol. Chem.* **276**, 7246–7257.

Sekino Y., Kojima N. and Shirao T. (2007) Role of actin cytoskeleton in dendritic spine morphogenesis. *Neurochem. Int.* **51**, 92–104.

Sharma S., Grintsevich E. E., Phillips M. L., Reisler E. and Gimzewski J. K. (2011) Atomic force microscopy reveals drebrin induced remodeling of f-actin with subnanometer resolution. *Nano Lett.* **11**, 825–827.

Sharma S., Grintsevich E. E., Hsueh C., Reisler E. and Gimzewski J. K. (2012) Molecular cooperativity of drebrin1-300 binding and structural remodeling of F-actin. *Biophys. J .* **103**, 275–283.

Shiraishi Y., Mizutani A., Yuasa S., Mikoshiba K. and Furuichi T. (2004) Differential expression of Homer family proteins in the developing mouse brain. *J. Comp. Neurol.* **473**, 582–599.

Shirao T. and Gonzalez-Billault C. (2013) Actin filaments and microtubules in dendritic spines. *J. Neurochem.* **126**, 155–164.

Shirao T. and Obata K. (1986) Immunochemical homology of 3 developmentally regulated brain proteins and their developmental change in neuronal distribution. *Brain Res.* **394**, 233–244.

Shirao T., Kojima N., Kato Y. and Obata K. (1988) Molecular cloning of a cDNA for the developmentally regulated brain protein, drebrin. *Brain Res.* **464**, 71–74.

Shirao T., Hayashi K., Ishikawa R., Isa K., Asada H., Ikeda K. and Uyemura K. (1994) Formation of thick, curving bundles of actin by drebrin A expressed in fibroblasts. *Exp. Cell Res.* **215**, 145–153.

Sholl D. A. (1953) Dendritic organization in the neurons of the visual and motor cortices of the cat. *J. Anat.* **87**, 387–406.

Takahashi H., Sekino Y., Tanaka S., Mizui T., Kishi S. and Shirao T. (2003) Drebrin-dependent actin clustering in dendritic filopodia governs synaptic targeting of postsynaptic density-95 and dendritic spine morphogenesis. *J. Neurosci.* **23**, 6586–6595.

Takahashi H., Mizui T. and Shirao T. (2006) Down-regulation of drebrin A expression suppresses synaptic targeting of NMDA receptors in developing hippocampal neurones. *J. Neurochem.* **97**(Suppl 1), 110–115.

Takeshita A., Yen P. M., Ikeda M., Cardona G. R., Liu Y., Koibuchi N., Norwitz E. R. and Chin W. W. (1998) Thyroid hormone response elements differentially modulate the interactions of thyroid hormone receptors with two receptor binding domains in the steroid receptor coactivator-1. *J. Biol. Chem.* **273**, 21554–21562.

Tohgi H., Utsugisawa K., Yamagata M. and Yoshimura M. (1995) Effects of age on messenger RNA expression of glucocorticoid, thyroid hormone, androgen, and estrogen receptors in postmortem human hippocampus. *Brain Res.* **700**, 245–253.

J Physiol 592.1 (2014) pp 229–247

Neuroscience

The Journal of Physiology

Kv3.3 channels harbouring a mutation of spinocerebellar ataxia type 13 alter excitability and induce cell death in cultured cerebellar Purkinje cells

Tomohiko Irie[1,2], Yasunori Matsuzaki[2], Yuko Sekino[1] and Hirokazu Hirai[2]

[1]*Division of Pharmacology, National Institute of Health Sciences, Setagaya 158-8501, Japan*
[2]*Department of Neurophysiology, Gunma University Graduate School of Medicine, Maebashi, Gunma, 371-8511, Japan*

Key points

- The cerebellum plays crucial roles in controlling sensorimotor functions, and patients with spinocerebellar ataxia type 13 exhibit cerebellar atrophy and cerebellar symptoms.
- The disease is an autosomal dominant disorder caused by missense mutations in the voltage-gated K^+ channel Kv3.3, which is expressed intensely in the cerebellar Purkinje cells, the sole output neurons from the cerebellar cortex.
- Here, we examined how these mutations cause the cerebellar disease by lentiviral expression of the mutant Kv3.3 in mouse cultured Purkinje cells.
- Expression of the mutant Kv3.3 suppressed outward currents, broadened action potentials and elevated basal intracellular calcium concentration in Purkinje cells. Moreover, the mutant-expressing Purkinje cells showed impaired dendrites and extensive cell death, both of which were significantly rescued by blockade of P/Q-type Ca^{2+} channels.
- These results suggest that Purkinje cells in the patients also exhibit similar abnormalities, which may account for the pathology of the disease.

Abstract The cerebellum plays crucial roles in controlling sensorimotor functions. The neural output from the cerebellar cortex is transmitted solely by Purkinje cells (PCs), whose impairment causes cerebellar ataxia. Spinocerebellar ataxia type 13 (SCA13) is an autosomal dominant disease, and SCA13 patients exhibit cerebellar atrophy and cerebellar symptoms. Recent studies have shown that missense mutations in the voltage-gated K^+ channel Kv3.3 are responsible for SCA13. In the rodent brain, Kv3.3 mRNAs are expressed most strongly in PCs, suggesting that the mutations severely affect PCs in SCA13 patients. Nevertheless, how these mutations affect the function of Kv3.3 in PCs and, consequently, the morphology and neuronal excitability of PCs remains unclear. To address these questions, we used lentiviral vectors to express mutant mouse Kv3.3 (mKv3.3) channels harbouring an R424H missense mutation, which corresponds to the R423H mutation in the Kv3.3 channels of SCA13 patients, in mouse cerebellar cultures. The R424H mutant-expressing PCs showed decreased outward current density, broadened action potentials and elevated basal $[Ca^{2+}]_i$ compared with PCs expressing wild-type mKv3.3 subunits or those expressing green fluorescent protein alone. Moreover, expression of R424H mutant subunits induced impaired dendrite development and cell death selectively in PCs, both of which were rescued by blocking P/Q-type Ca^{2+} channels in the culture conditions. We therefore concluded that expression of R424H mutant subunits in PCs markedly affects the function of endogenous Kv3 channels, neuronal excitability and, eventually, basal $[Ca^{2+}]_i$, leading to cell death. These

DOI: 10.1113/jphysiol.2013.264309

results suggest that PCs in SCA13 patients also exhibit similar defects in PC excitability and induced cell death, which may explain the pathology of SCA13.

(Received 28 August 2013; accepted after revision 5 November 2013; first published online 11 November 2013)
Corresponding authors T. Irie: Division of Pharmacology, National Institute of Health Sciences, 1-18-1 Kamiyoga, Setagaya-ku, Tokyo 158-8501, Japan. Email: irie@nihs.go.jp or H. Hirai: Department of Neurophysiology, Gunma University Graduate School of Medicine, 3-39-22 Shouwa-machi, Maebashi-shi, Gunma 371-8511, Japan. Email: hirai@gunma-u.ac.jp

Abbreviations ACSF, artificial cerebrospinal fluid; AF, AlexaFluor; a.u., arbitrary unit; calbindin, calbindin D-28k; DIV, days *in vitro*; DNQX, 6,7-dinitroquinoxaline-2,3-dione; *G*, conductance; GFP, green fluorescent protein; hKv3.3, human Kv3.3; I_{Na}, Na^+ current; *k*, a slope factor; mKv3.3, mouse Kv3.3; MSCV, murine embryonic stem cell virus; PBS-XCG, PBS containing 0.3% Triton X-100, 0.12% λ-carrageenan, 1% goat serum and 0.02% sodium azide; PCs, Purkinje cells; P2A, 2A peptide sequence from porcine teschovirus-1; R_{max}, maximal fluorescence ratio; R_{min}, minimal fluorescence ratio; RT, room temperature; SCA13, spinocerebellar ataxia type 13; sEPSCs, spontaneous excitatory postsynaptic currents; τ_{acti}, activation time constant; τ_{inacti}, inactivation time constant; τ_{recove}, recovery time constant; VSV-G, vesicular stomatitis virus G protein; WT, wild-type.

Introduction

In most excitable cells, the high K^+ permeability arises from delayed-rectifier K^+ channels of the Kv class (Hille, 2001). One of the Kv subfamilies, known as Kv3, has generated particular interest because of its unique electrophysiological properties (Rudy & McBain, 2001). The Kv3 channels are high-voltage-activated K^+ channels, and they exhibit fast activation and deactivation kinetics; therefore, Kv3 channels are activated during action potential depolarization and are indispensable for high-frequency firing in many neurons, such as fast-spiking cortical interneurons and cerebellar Purkinje cells (PCs; Erisir *et al.* 1999; McKay & Turner, 2004). Rodents and humans possess four Kv3 genes: *Kv3.1–3.4*. The Kv3 channels are composed of four pore-forming subunits and form heterotetrameric channels by combination of Kv3 members. In the rodent brain, Kv3.3 mRNA and protein are abundantly expressed in the cerebellum, in which the mRNA is most intensely expressed in PCs (Weiser *et al.* 1994; Chang *et al.* 2007). Interestingly, Kv3.3-deficient mice show normal PC morphology and no ataxic phenotype (Joho *et al.* 2006; Hurlock *et al.* 2008; Zagha *et al.* 2010).

The numerous diseases arising from channel dysfunction (channelopathies) illustrate the importance of ion channels to the organism. To date, missense mutations in more than 60 ion-channel genes have been associated with human disease (Ashcroft, 2006). Recently, missense mutations in the *KV3.3* gene (also known as *KCNC3*), which encodes human Kv3.3 (hKv3.3) channels, were linked to autosomal dominant spinocerebellar ataxia type 13 (SCA13). Spinocerebellar ataxia type 13 is accompanied by cerebellar symptoms and by cerebellar atrophy, and three different mutations (R420H, R423H and F448L) have been identified, although the neurodegenerative changes in the post-mortem cerebellum have not been investigated (Waters *et al.* 2006; Figueroa *et al.* 2010). In *Xenopus* oocyte expression systems, coexpression of the R420H or R423H mutant subunits with wild-type (WT) hKv3.3 suppresses the current by a dominant-negative mechanism. Given the intense Kv3.3 expression in rodent PCs and the cerebellar atrophy in SCA13 patients, these mutations are expected to affect the neuronal excitability and morphology of PCs severely. Recently, Issa *et al.* reported that zebrafish expressing mutant zebrafish Kv3.3 subunits (homologous to the F448L mutant) in spinal motoneurons, which endogenously express Kv3.3, show defective axonal pathfinding (Issa *et al.*, 2012). However, as they used a motoneuron-specific enhancer to drive expression, these zebrafish display no distinct cerebellar abnormality. Therefore, the pathology of SCA13 has not been elucidated, and other methodological approaches are needed.

In the present study, to investigate the effects of *Kv3.3* mutations in PCs, we expressed mouse Kv3.3 (mKv3.3) channels harbouring the R424H missense mutation, which corresponds to the R423H mutation in hKv3.3, using a lentivirus system in mouse cerebellar cultures. Immunohistochemical analysis revealed that expression of R424H mutant subunits induced impaired dendrite development and cell death in PCs by 11 days *in vitro* (DIV) without significant alteration in granule cells. To examine the effects of R424H mutant subunits on the electrophysiological properties and free $[Ca^{2+}]_i$ of PCs, we performed whole-cell patch-clamp recordings and calcium imaging from PCs at DIV 8–10. Action potential duration and basal $[Ca^{2+}]_i$ were significantly increased in R424H mutant-expressing PCs compared with PCs expressing WT mKv3.3 or those expressing green fluoresent protein (GFP) alone. Furthermore, blockade of P/Q-type Ca^{2+} channels by ω-agatoxin IVA in the culture conditions rescued the dendritic maldevelopment and cell death in PCs caused by R424H mutant subunits.

Methods

Ethical approval

Newborn (i.e. within 24 h after birth) mice (ICR strain) of both sexes were used for cerebellar cultures. *Xenopus* oocytes were collected from anaesthetized *Xenopus laevis*. These animals were used according to the Guiding Principles for the Care and Use of Laboratory Animals approved by the guidelines of the National Institute of Health Sciences, Japan. All experiments also complied with *The Journal of Physiology* policy and UK regulations on animal studies (Drummond, 2009).

Molecular biology

The mouse cerebellum expresses the *Kv3.3b* gene, which is an alternatively spliced isoform of *mKv3.3* (Goldman-Wohl *et al.* 1994). *mKv3.3* cDNA that is nearly identical to *Kv3.3b* (Desai *et al.* 2008) was obtained as a kind gift from Dr Leonard K. Kaczmarek (Yale University, New Haven, CT, USA). The amino acid identity between hKv3.3 (Gene Accession number: AF055989) and mKv3.3 is 89%, and the sequence of the S4 transmembrane segment showed a complete match between the two species (Supplemental Fig. S1). To date, several reports have shown that there are three types of missense mutations (R420H, R423H and F448L) in hKv3.3 channels in distinct SCA13 pedigrees (Waters *et al.* 2006; Figueroa *et al.* 2010, 2011). In the present study, we focused on the R423H mutation. The S4 transmembrane segment of mKv3.3 has an arginine residue at position 424, which corresponds to the arginine at position 423 in hKv3.3. The arginine of mKv3.3 was replaced with histidine by overlap PCR using PrimeSTAR HS DNA Polymerase (Takara Bio, Shiga, Japan). The nucleotide exchanges were c.1271G>A and c.1272T>C. Wild-type and R424H mutant *mKv3.3* cDNA were subcloned in pcDNA3 (Invitrogen, Carlsbad, CA, USA), and the mutation was confirmed by sequencing.

For lentiviral vector-based gene expression, the murine embryonic stem cell virus (MSCV) promoter, which drives PC-predominant expression of a transgene in cerebellum, was used (Hawley *et al.* 1994; Hanawa *et al.* 2004; Torashima *et al.* 2006; Takayama *et al.* 2008). A Kozak translation initiation sequence and 2A peptide sequence from porcine teschovirus-1 (P2A) for efficient cleavage of polyproteins were placed at the N- and C-termini of WT and R424H mutant *mKv3.3* cDNA, respectively (Szymczak *et al.* 2004; Torashima *et al.* 2009). Then, stop codons were removed using the following PCR primer pair: a 5′ primer with an *Age*I site and Kozak sequence (bold; 5′ primer, CGACCGGT**GCCACC**ATGCT CAGTTCAGTGTGCGT) and a 3′ primer with an *Age*I site and P2A (bold; 3′ primer, CGACCGGT**GGCCCGG GTTTTCTTCAACATCTCCTGCTTGCTTTAACAGAG AGAAGTTCGTGGC**GCCGGAGCCGAGGATGGAGGG CAGGGTCG). A Gly-Ser-Gly linker (underlined in the 3′ primer) was also placed between the N-terminus of a WT (or R424H mutant) mKv3.3 sequence and P2A using the 3′ primer. This linker improves the cleavage efficacy of the P2A (Szymczak *et al.* 2004). The PCR products were subcloned in-frame into the *Age*I site of pCL20c MSCV-GFP, which is present 8 bp upstream from the translation initiation site of GFP. Finally, lentiviral transfer vectors for the experiments (pCL20c MSCV-WT-P2A-GFP and pCL20c MSCV-R424H-P2A-GFP) were obtained, and the inserted sequences were verified by sequencing.

Lentiviral vector preparation

Vesicular stomatitis virus G protein (VSV-G) pseudotyped lentiviral vector particles were produced by transient transfection of HEK 293T cells with viral plasmids as described previously (Torashima *et al.* 2006). In brief, HEK 293T cells were transfected with a mixture of the following four plasmids: pCAGkGP1R, pCAG4RTR2, pCAG-VSV-G and the lentiviral transfer vector plasmid (pCL20c MSCV-GFP, pCL20c MSCV-WT-P2A-GFP or pCL20c MSCV-R424H-P2A-GFP). The medium containing viral particles was concentrated by ultracentrifugation and resuspended in 70 μl of Dulbecco's phosphate-buffered saline (Wako Pure Chemical Industries, Osaka, Japan). The infectious titres of the virus were determined as follows: virus stocks were added to HEK 293T cells in the presence of Polybrene (6 μg ml^{-1}; Sigma-Aldrich, St Louis, MO, USA). After 4 days, GFP-positive cells were counted using a Tali Image-Based Cytometer (Invitrogen), and the titres were adjusted to 1.0×10^{10} or 0.5×10^{10} transduction units/ml.

Cerebellar culture and lentivirus-mediated gene expression

Cerebellar cultures were prepared according to our previous protocol with some modifications (Hirai & Launey, 2000). After the mice were killed by decapitation, the cerebella of newborn mice were quickly removed and treated with 2 ml of a papain digestion solution containing 40 units of papain (Worthington Biochemical, Lakewood, NJ, USA), 2 mM L-cysteine hydrochloride and 1 mM EDTA in Ca^{2+}–Mg^{2+}-free Hank's balanced salt solution (pH 7.0; Gibco, Grand Island, NY, USA; Tabata *et al.* 2000). Then, the cerebella were dissociated by trituration in Hank's balanced salt solution containing 0.05% (w/v) DNase (Sigma-Aldrich) and 12 mM $MgSO_4$. After centrifugation (180 × *g*, 5 min), the cells were resuspended in DMEM/F12 (Gibco)-based medium containing 4.2 mM

KCl, 1% (v/v) horse serum, 2% (v/v) B-27 (Gibco) and a mixture of a penicillin–streptomycin solution (1000 U ml^{-1} and 100 mg ml^{-1}, respectively; Gibco) to a density of 10×10^6 cells ml^{-1} (Gimenez-Cassina *et al.* 2007). High (25 mM)-KCl-containing medium, which is often used for rat cerebellar cultures, was not used in this study because low (5 mM)-KCl-containing medium can improve the long-term viability of mouse cerebellar granule cells, and high-KCl medium maintains the gene expression patterns of granule cells in an immature condition (Mellor *et al.* 1998; Sato *et al.* 2005). A mixture of the cell suspension (20 μl) and the concentrated virus solution (1 μl) was plated onto plastic coverslips (Cell Desk LF1, Sumilon MS-92132; Sumitomo Bakelite, Tokyo, Japan) coated with poly-D-lysine (Sigma-Aldrich) and incubated for 10 h in a CO_2 incubator for virus infection. The DMEM/F12-based medium (700 μl) was added to each dish and replaced by half once a week. Green fluorescent protein fluorescence was first observed at DIV 3, and its expression continued thereafter. In some experiments, ω-agatoxin IVA (0.2 μM; Peptide Institute, Tokyo, Japan), a P/Q-type Ca^{2+} channel blocker, was added to the culture medium every other day from DIV 2 (Mintz & Bean, 1993; Mikuni *et al.* 2013).

Histochemical examination

Cerebellar cultures were fixed in 4% (w/v) formaldehyde in PBS (pH 7.4) for 30 min at room temperature (RT) and incubated overnight at 4°C in PBS containing 0.3% Triton X-100, 0.12% λ-carrageenan, 1% goat serum and 0.02% sodium azide (PBS-XCG) with the following combination of primary antibodies: guinea-pig polyclonal anti-GFP antibody (1:1000 dilution, GFP-GP-Af1180-1; Frontier Institute, Hokkaido, Japan), rabbit polyclonal anti-calbindin D-28K antibody (1:2000 dilution, AB1778; Millipore, Billerica, MA, USA; calbindin is a marker protein of PCs) and mouse monoclonal anti-NeuN antibody (1:2000 dilution, MAB377; Millipore) in PBS-XCG. The samples were further incubated for 3 h at RT in PBS-XCG with the following secondary antibodies: AlexaFluor (AF) 488-conjugated goat anti-guinea-pig IgG antibody (A-11073; Invitrogen), AF 568-conjugated goat anti-rabbit IgG antibody (A-11011; Invitrogen) and AF 680-conjugated goat anti-mouse IgG antibody (A-21058; Invitrogen) in PBS-XCG. All secondary antibodies were used at a concentration of 5 μg ml^{-1}. For examination of nuclear morphology, some cerebellar cultures were stained with Hoechst 33342 (1 μg ml^{-1} in PBS; Dojindo, Kumamoto, Japan) for 15 min at RT after the secondary antibody treatment.

Immunofluorescence was observed under a confocal microscope (A1R; Nikon, Tokyo, Japan) with the following appropriate filter sets: Hoechst 33342 (excitation, 403 nm; emission, 425–475 nm), AF 488 (excitation, 488 nm; emission, 500–550 nm), AF 568 (excitation, 561 nm; emission, 570–620 nm) and AF 680 (excitation, 639 nm; emission, 662–737 nm). Images were obtained with ×10 objective or ×60 water-immersion objective lenses. The confocal pinhole size was 1.0 airy unit. In some experiments, dendrites of PCs were traced from calbindin-positive areas using Neurolucida software (MBF Bioscience, Burlington, VT, USA). The extension of dendritic trees and dendrite complexity were measured by Sholl analysis in Neuroexplorer software (MBF Bioscience; Sholl, 1953; Sawada *et al.* 2010). Concentric spheres were centred on the cell body, and the radii were incremented by 10 μm. The number of branching points within each sphere was counted, and total dendritic length was measured. The cell densities of PCs and granule cells were calculated in each culture by averaging four values of cell density measured from a single image obtained around the centre of the culture with a ×10 objective lens. These measurements were performed using NIS-Elements AR 3.2 software (Nikon).

Data are provided as the means ± SD, and n is the number of experiments. Statistical significance was tested using the Mann–Whitney U test unless otherwise stated (significance, $P < 0.05$). GraphPad Prism 5 (GraphPad Software, San Diego, CA, USA) and StatView 5 software (SAS Institute, Cary, NC, USA) were used for the analysis. In Figs 2–4 and 6–8 and Tables 1 and 2, statistical analysis was performed between cells expressing the R424H mutant and those expressing GFP alone or between cells expressing the R424H mutant and those expressing WT mKv3.3.

Expressions of heterologous proteins in *Xenopus* oocytes

The detailed procedures have been described previously (Kubo & Murata, 2001). Briefly, linearized WT or R424H mutant cDNA in pcDNA3 was used as a template to produce capped cRNA using T7 RNA polymerase (mMESSAGE mMACHINE; Ambion, Austin, TX, USA). *Xenopus* oocytes were collected from frogs anaesthetized in water containing 0.15% (w/v) tricaine. The isolated oocytes were treated with collagenase (2 mg ml^{-1}; type 1; Sigma-Aldrich) and injected with 50 nl of nuclease-free water containing 10 ng of WT *mKv3.3* cRNA, a mixture of 10 ng of WT and 10 ng of R424H mutant cRNAs, or 10 ng of R424H mutant cRNA. The oocytes were then incubated at 17°C in frog Ringer solution containing (mM): 88 NaCl, 1 KCl, 2.4 $NaHCO_3$, 0.3 $Ca(NO_3)_2$, 0.41 $CaCl_2$ and 0.82 $MgSO_4$, pH 7.6, with 0.1% (v/v) penicillin–streptomycin solution (Sigma-Aldrich) for 2–3 days before recordings.

Electrophysiological recording from *Xenopus* oocytes

Potassium currents were recorded under a two-electrode voltage clamp using an OC-725C amplifier (Warner Instruments, Hamden, CT, USA) and Clampex 10.3 software (Molecular Devices, Sunnyvale, CA, USA). The signals were digitized at 10 kHz using a Digidata 1322A (Molecular Devices). The microelectrodes were filled with an electrode solution containing 3 M potassium acetate and 10 mM KCl. The oocytes were perfused with a bath solution containing (mM): 96 NaCl, 2 KCl, 1.8 $CaCl_2$, 1 $MgCl_2$ and 5 Hepes (pH adjusted to 7.2 with NaOH). All experiments were performed at 25°C. The data were analysed using Clampfit 10.3 software (Molecular Devices) and Igor Pro 6 software (Wavemetrics, Lake Oswego, OR, USA) with the added import functionality provided by the ReadPclamp XOP of the NeuroMatic software package (http://www.neuromatic.thinkrandom.com/). To calculate conductance–voltage relationships, outward currents were activated by applying 1000 ms voltage steps from a holding potential of −80 mV to potentials up to +70 mV in 10 mV increments. The equilibrium potential of K^+ ($E_K = -104.0$ mV) was calculated from the intracellular concentration of K^+ (109.5 mM) in the *Xenopus* oocyte (Costa *et al.* 1989). To determine steady-state inactivation, cells were held at −80 mV before applying a 1000 ms prepulse to potentials between −80 and +60 mV in 10 mV increments, followed by a 250 ms test pulse to +20 mV. Steady-state inactivation (I/I_{max}) curves were fitted with the Boltzmann function, $I/I_{max} = 1/[1 + \exp(V - V_{\frac{1}{2}})/k]$, where k is a slope factor. To measure the rates of deactivation, outward currents were evoked by stepping from a holding potential of −80 mV to +50 mV for 5 ms and then stepping to potentials between −60 and +10 mV in 10 mV increments for 50 ms. The time constant of recovery (τ_{recove}) from inactivation was determined by depolarizing the cells to +50 mV for 1000 ms from a holding potential of −80 mV. A step to −80 mV of variable duration was followed with test pulses to +50 mV for 200 ms in 500 ms increments. The data points were fitted with a single exponential function. The time constants of inactivation (τ_{inacti}) and deactivation were obtained by fitting current traces with a single exponential function on the inactivating and deactivating phases of the traces, respectively.

Whole-cell patch-clamp recordings from cultured PCs

In most recordings, cerebellar cultures were constantly perfused (2 ml min^{-1}) with oxygenated artificial cerebrospinal fluid (ACSF) containing (mM): 120 NaCl, 2.5 KCl, 2 $CaCl_2$, 1 $MgCl_2$, 26 $NaHCO_3$, 1.25 NaH_2PO_4, 17 D-glucose and 0.1 picrotoxin (Tocris Bioscience, Bristol, UK; a $GABA_A$ receptor antagonist), bubbled with 5% CO_2–95% O_2 at 26°C. The other recordings were performed in Hepes-buffered ACSF containing (mM): 140 NaCl, 2.5 KCl, 2 $CaCl_2$, 1 $MgCl_2$, 10 D-glucose and 10 Hepes (pH adjusted to 7.4 with NaOH), bubbled with 100% O_2. Outward currents were recorded in Hepes-buffered ACSF containing (mM): 0.2 $CdCl_2$, 0.1 picrotoxin, 0.05 6,7-dinitroquinoxaline-2,3-dione (DNQX; Tocris Bioscience; a AMPA/kainate receptor antagonist,) and 0.001 TTX (Wako Pure Chemical Industries). Hepes buffer was used to avoid the precipitation of $CdCO_3$.

Cells were visualized on the stage of an upright microscope (BX50WI; Olympus, Tokyo, Japan) using a ×40 water-immersion objective lens with Nomarski optics and a near-infrared CCD camera (C-3077-79; Hamamatsu Photonics, Hamamatsu, Japan). Green fluorescent protein-positive cells were visualized and selected using epifluorescence optics (Olympus). Patch pipettes were made from borosilicate glass capillaries to reduce pipette capacitance (GC150F-100; Harvard Apparatus, Holliston, MA, USA) and had a resistance of 1.5–2.5 MΩ when filled with a potassium gluconate-based internal solution containing (mM): 145 potassium gluconate, 5 KCl, 0.1 EGTA, 5 Mg-ATP, 5 disodium phosphocreatine, 0.3 Na_2-GTP, 10 Hepes–KOH and 10 biocytin (Sigma-Aldrich), pH 7.3. The liquid junction potential (−10 mV) was corrected offline. Whole-cell patch-clamp recordings were conducted in GFP-positive PCs at DIV 8–10. Purkinje cells were identifiable by their large somatic size (Tabata *et al.* 2000), and their identity was confirmed by intracellular staining with biocytin. Patch-clamp recordings were acquired using a Multiclamp 700B amplifier with Clampex 10.3 software (Molecular Devices). Signals were filtered at 6–10 kHz and digitized at 10–50 kHz using a Digidata 1440A (Molecular Devices). In voltage-clamp conditions, series resistance was compensated electronically by 80–90%, and in current-clamp conditions, it was performed using the bridge balance and capacitance neutralization. Outward currents were activated with 500 ms voltage steps from −70 mV to voltages ranging from −60 to +40 mV in 10 mV increments. Leak currents were subtracted online by the *P*/4 protocol (Armstrong & Bezanilla, 1974). The recorded currents were normalized to cell capacitance, which was calculated from the transient current evoked by applying a small voltage step (−5 mV, 20 ms duration) from a holding potential of −70 mV in voltage-clamp conditions. Spontaneous excitatory post-synaptic currents (sEPSCs) were recorded at a holding potential of −80 mV for 250 s in the presence of picrotoxin and detected offline using the template search function in the Clampfit 10.3 software. Action potentials were evoked by depolarizing current pulses in current-clamp conditions (10 ms duration, from 0 to 200 pA in 10 pA increments; or 200 ms duration, from 0 to 200 pA in 20 pA increments). The resting membrane potentials were

adjusted to −60 mV by current injection. Spontaneous firing was recorded at resting membrane potential for 300 s. The half-amplitude width of the action potential was measured at the mid-point between the threshold and peak. Action potential amplitude was measured between the threshold and peak.

Fluorescence imaging of calcium

To monitor the free $[Ca^{2+}]_i$ of PCs, cerebellar cultures at DIV 8–10 were incubated with Hepes-buffered ACSF containing fura-2 AM (0.01 mM; Invitrogen) for 1 h at 37°C. The cells were visualized and perfused with Hepes-buffered ACSF at the same settings as those used for the patch-clamp recordings. For fura-2 excitation, the cultures were illuminated alternately at 340 and 380 nm wavelengths using a 100 W xenon lamp source, a fura-2 filter set (ET FURA2; Chroma Technology, Brattleboro, VT, USA), and a filter wheel (Ludl Electronic Products, Hawthorne, NY, USA). The fluorescence was filtered through a bandpass filter (470–550 nm) and captured using an EMCCD camera (iXon3 DU897; Andor Technology, Belfast, UK). The experiments were controlled by Andor iQ software (Andor Technology). The regions of interest were defined as the shape of the GFP-expressing Purkinje cell bodies. The $[Ca^{2+}]_i$ was calculated according to the previously described method with a dissociation constant of 224 nM (Grynkiewicz *et al.* 1985). The maximal and minimal fluorescence ratios (R_{max} and R_{min}) were measured after addition of the calibration solutions. The R_{max} was measured in Hepes-buffered ACSF containing 5 μM ionomycin (Sigma-Aldrich), and R_{min} in Hepes-buffered, Ca^{2+}-free ACSF containing 10 mM EGTA and 5 μM ionomycin. In some experiments, the cultures were perfused for 5 min with high-K^+ ACSF, in which 12.5 mM NaCl was replaced by equimolar KCl (total $[K^+]$, 15 mM) to elevate $[Ca^{2+}]_i$. Basal $[Ca^{2+}]_i$ was obtained as an average for a 7 min period from the beginning of the recordings, and elevated $[Ca^{2+}]_i$ for a 5 min period during high-K^+ ACSF perfusion.

Results

R424H mutant subunits exhibit a dominant-negative effect against WT mKv3.3 subunits without affecting WT subunit expression in heterologous expression systems

We examined whether the biophysical properties of hKv3.3 with the R423H mutation were conserved in mKv3.3 with the R424H mutation using the *Xenopus* oocyte expression system and two-electrode voltage-clamp recording (Figueroa *et al.* 2010; Minassian *et al.* 2012). In WT mKv3.3-expressing oocytes, depolarizing voltage steps from a holding potential of −80 mV evoked outward currents that became more apparent when the membrane was depolarized to potentials more positive than −10 mV (Supplemental Fig. S2*Aa* and S2*C*; a $V_{1/2}$ of activation of 25.5 ± 3.1 mV, $n = 19$), and the currents showed inactivation (Supplemental Fig. S2*Aa*, $n = 11$) and fast deactivation (deactivation $\tau = 0.948 \pm 0.15$ ms at −40 mV, $n = 11$; trace not shown). These results well reflected the reported properties of Kv3.3 channels, i.e. fast activation, positively shifted voltage dependence, N-type inactivation and a fast deactivation rate (Rae & Shepard, 2000; Rudy & McBain, 2001; Desai *et al.* 2008). In R424H mutant-expressing oocytes, negligible currents were observed at potentials more positive than +20 mV (Supplemental Fig. S2*Ac* and S2*B*), and the peak amplitudes were not significantly larger than those recorded in water-injected oocytes (Supplemental Fig. S2*B*; not significant by Student's unpaired *t* test), indicating that most of the currents were derived from endogenous channels present in *Xenopus* oocytes. When cRNA of WT and R424H mutant mKv3.3 was injected at a 1:1 ratio (WT+R424H), the $V_{1/2}$ of activation was significantly left-shifted, by 9.05 mV, compared with oocytes expressing WT subunits alone (Supplemental Fig. S2*C*; WT+R424H, 15.6 ± 9.2 mV, $n = 21$; WT, 24.6 ± 6.1 mV, $n = 19$; $P < 0.001$ by Student's unpaired *t* test). The value of k was decreased by 4.29 mV (WT + R424H, $k = 9.82 \pm 2.4$ mV, $n = 21$; WT, $k = 14.1 \pm 3.1$ mV, $n = 19$; $P < 0.001$ by Student's unpaired *t* test), and the time constant of activation (τ_{acti}) at +40 mV was 2.03-fold slower (Supplemental Fig. S2*Da* and S2*Db*; $P < 0.001$ by Student's unpaired *t* test). These results are consistent with previous reports of hKv3.3 with R423H mutation (Figueroa *et al.* 2010; Minassian *et al.* 2012) and indicate that the functional effects of this mutation are well conserved between humans and mice.

Coexpression of R424H mutant and WT subunits accelerates the inactivation kinetics and slows the recovery from inactivation compared with WT subunits alone

In order to reveal further the unknown biophysical properties of hKv3.3 with the R423H mutation, we investigated the inactivation kinetics, steady-state inactivation and recovery from inactivation of WT+R424H mutant channels. The τ_{inacti} of WT+R424H mutant channels was more than 2-fold faster than that of channels composed of WT subunits alone in the range of +10 to +70 mV depolarizing steps (Fig. 1*A*), and the $V_{1/2}$ of inactivation was significantly left-shifted, by 9.67 mV, compared with that of WT subunits (Fig. 1*B*; WT+R424H, $V_{1/2} = -4.39 \pm 7.09$ mV, $n = 12$; WT, $V_{1/2} = 5.28 \pm 5.33$ mV, $n = 11$; $P < 0.01$ by

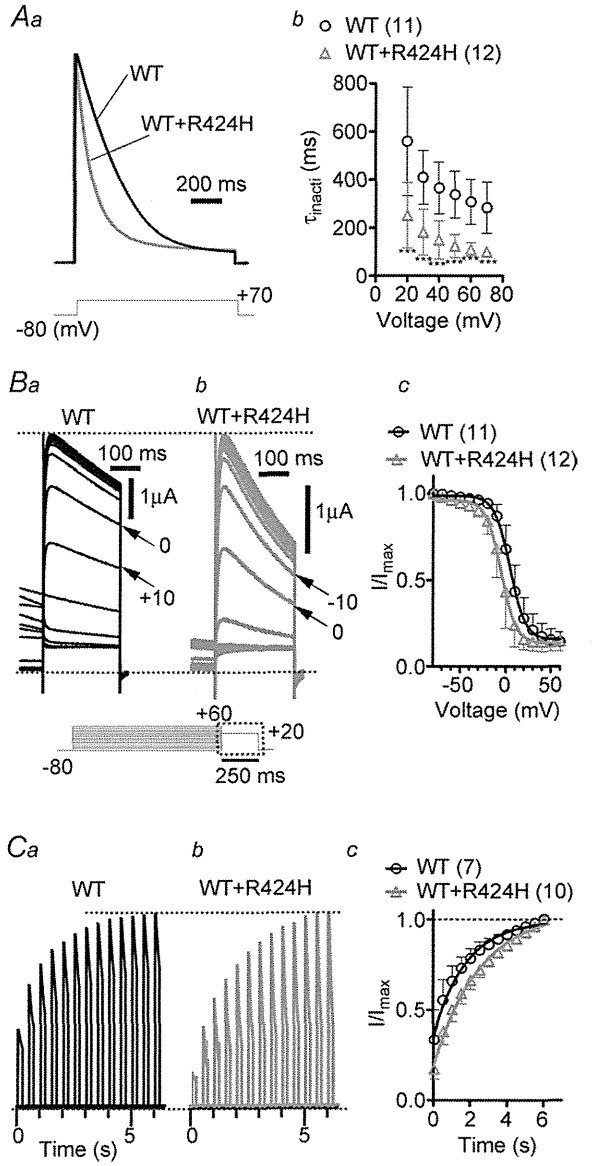

Figure 1. Coexpression of R424H mutant and wild-type (WT) subunits in *Xenopus* oocytes accelerates the inactivation kinetics and slows the recovery from inactivation compared with WT subunits alone

Aa, representative traces evoked by stepping from a −80 mV holding potential to +70 mV. The current traces are scaled to the same peak amplitude. *Ab*, the plots of the inactivation time constant (τ_{inacti}) were determined by fitting the falling phases of currents obtained in Supplemental Fig. S2*A* with a single exponential function. *Ba* and *b*, comparison of steady-state inactivation, which was obtained by changing the membrane potential from a prepulse potential ranging from −80 to +60 mV in 10 mV increments to a test voltage step of +20 mV to record tail currents. *Ba* and *b* shows traces of tail currents, and their corresponding voltage pulses are given under the traces surrounded by the dotted rectangle. *Bc*, the tail current amplitudes were normalized to the maximal current, and the resulting plots were fitted with the Boltzmann function, $I/I_{max} = 1/[1 + \exp(V - V_{1/2})/k]$, where k is a slope factor. *C*, recovery from inactivation in WT channels and WT+R424H mutant channels. *Ca* and *b*, the recovery time constant (τ_{recove}) was determined by depolarizing the cells to +50 mV for 1000 ms from a holding potential of −80 mV. A step to −80 mV of variable duration was followed with test pulses to +50 mV for 200 ms in 500 ms increments. *Cc*, time course of the recovery from inactivation. The curves were fitted with a single exponential function to obtain τ_{recove}. Here and in the following figures, error bars indicate standard deviation, the numbers in parentheses indicate the number of experiments, and statistical significance was tested using Mann-Whitney's *U* test unless otherwise stated (significance, $P < 0.05$). ***$P < 0.001$.

Student's unpaired *t* test). The τ_{recove} from inactivation of WT+R424H was significantly slower than that of WT (Fig. 1*C*; WT+R424H, $\tau_{recove} = 2.62 \pm 0.60$, $n = 10$; WT, $\tau_{recove} = 1.78 \pm 0.08$, $n = 7$; $P < 0.01$ by Student's unpaired *t* test). These results indicate that coexpression of WT and R424H mutant subunits accelerated the inactivation kinetics and slowed recovery from inactivation.

Expression of R424H mutant subunits in cerebellar cultures induces PC death and impairs dendritic development

Spinocerebellar ataxia type 13 patients show cerebellar symptoms and cerebellar atrophy, suggesting shrinkage of the cerebellar cortex and degeneration of cerebellar neurons (Waters *et al.* 2006; Figueroa *et al.* 2010, 2011). In order to explore the effects of the R424H mutant on cell survival, dendritic development and electrophysiological properties in cerebellar neurons, mouse cerebellar cultures were infected at DIV 0 with lentiviruses expressing WT or R424H mutant subunits together with GFP. Given that SCA13 is an autosomal dominant disorder and Kv3 channels are formed by the assembly of four pore-forming subunits, hKv3.3 channels in SCA13 patients are considered to be heteromultimer channels consisting of WT and mutant subunits (MacKinnon, 1991; Figueroa *et al.* 2010; Minassian *et al.* 2012). When R424H mutant subunits were lentivirally expressed in cultured PCs, the subunits were expected to incorporate into endogenous mKv3.3 channels, mimicking the pathological condition.

Green fluorescent protein fluorescence was observed after DIV 3, and >90% of PCs were GFP positive (Fig. 2*A*–*C*). In the immunohistochemical experiments, PCs were immunostained with anti-calbindin antibody and granule cells with anti-NeuN antibody. Mullen *et al.* (1992) reported that PCs are not stained with anti-NeuN antibody *in vivo*. In agreement with their report, PCs and GABAergic interneurons were NeuN negative in our culture conditions (Supplemental Fig. S3*A* and S3*B*). The mKv3.3 protein in WT-expressing PCs at DIV 10 was significantly overexpressed (by 8.3-fold) compared with that in PCs expressing GFP alone (Supplemental Fig. S3*E*). In contrast to the clear expression of mKv3.3 protein

in PCs (Goldman-Wohl *et al.* 1994), mKv3.3 expression was not detected in cultured granule cells (Supplemental Fig. S3*C*), differing from a previous report using an *in vivo* preparation (Chang *et al.* 2007). Consistent with a previous report (Tabata *et al.* 2000), the relative densities of GFP- and WT-expressing PCs decreased in a day-dependent manner (Fig. 2*A*, *B* and *D*). Until DIV 7, the relative densities of PCs did not differ significantly between R424H mutant-expressing and control cultures (Fig. 2*Aa*, *Ba*, *Ca* and *D*; $P = 0.346$ between GFP and R424H; $P = 0.222$ between WT and R424H). At DIV 11, however, the density of PCs in R424H mutant-expressing cultures was significantly decreased (Fig. 2*Ab*, *Bb*, *Cb* and *D*; $P < 0.01$ between GFP and R424H; $P < 0.01$ between WT and R424H). At DIV 14, ~40% of PCs still survived in GFP- or WT-expressing cultures (Fig. 2*Ac*, *Bc*, *Cc* and *D*), whereas there were few surviving PCs in R424H mutant-expressing cultures. Relative cell densities and the percentage of GFP-positive cells of granule cells at DIV 14 were also quantified, but there were no significant differences between R424H mutant-expressing and control cultures (Fig. 2*Ac′*, *Bc′*, *Cc′* and *E*; cell densities, $P = 0.0952$ between GFP and R424H; $P = 0.117$ between WT and R424H; and percentage of GFP-positive cells, GFP, 65.9 ± 8.3%, $n = 5$; WT, 64.0 ± 7.4%, $n = 5$; R424H, 59.8 ± 8.1%, $n = 5$; $P = 0.421$ between GFP and R424H; $P = 0.310$ between WT and R424H), indicating that expression of R424H mutant subunits did

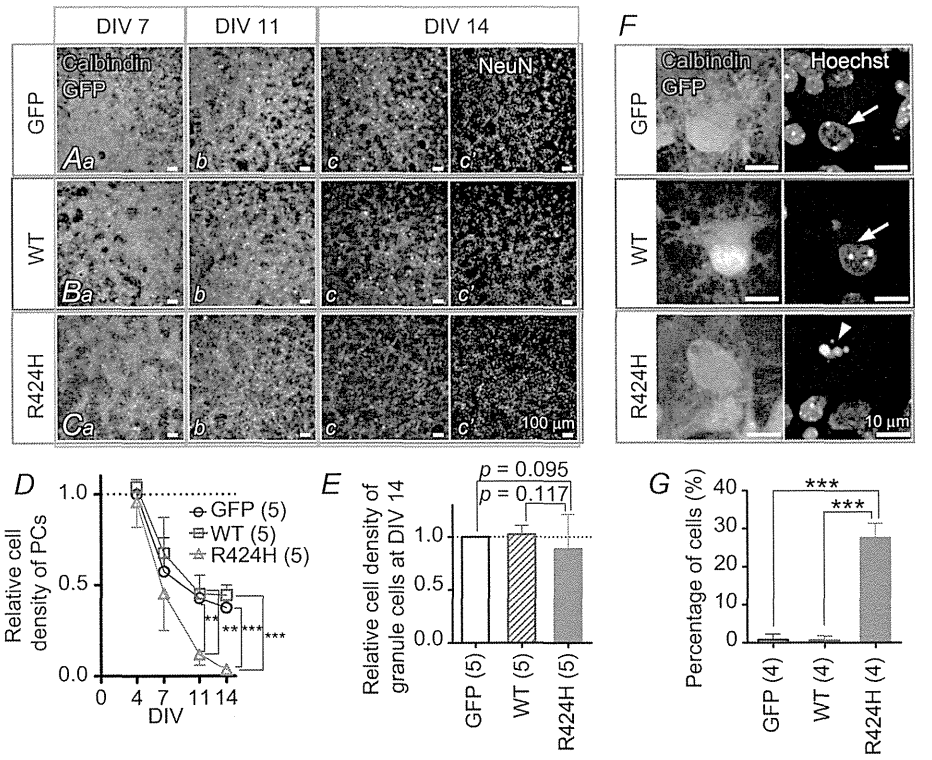

Figure 2. Lentivirus-mediated expression of R424H mutant subunits in cerebellar cultures decreases the density of Purkinje cells (PCs) but not of granule cells

A–C, immunofluorescence images of cerebellar cultures infected with lentiviral vectors expressing green fluorescent protein (GFP) alone (*Aa–c*), WT subunits and GFP (*Ba–c*) or R424H mutant subunits and GFP (*Ca–c*; see Methods). Green fluorescent protein fluorescence was enhanced by immunostaining with guinea-pig anti-GFP antibody and AlexaFluor (AF) 488-conjugated goat anti-guinea-pig antibody. Purkinje cells were visualized by immunolabelling with rabbit anti-calbindin antibody (red signals in *A–C*). *Ac′*, *Bc′* and *Cc′*, granule cells were selectively immunolabelled with mouse anti-NeuN mouse antibody (see Supplemental Fig. S3*A* and *B*). *D*, relative cell density of PCs plotted as a function of days *in vitro* (DIV). The density was normalized to the value of PCs expressing GFP alone at DIV 4. *E*, relative cell density of granule cells at DIV 14. The density was normalized to the mean cell density of granule cells in cultures lentivirally expressing GFP alone at DIV 14. *F* and *G*, R424H mutant-expressing PCs exhibiting chromatin condensation. *F*, representative fluorescence images of PCs at DIV 8. For nucleus detection, the PCs were stained with Hoechst 33342. Normal nuclei of PCs are indicated by arrows (GFP and WT), whereas a nucleus exhibiting chromatin condensation is marked with an arrowhead (R424H). *G*, summary of the percentages of PCs with chromatin condensation at DIV 8. The statistical analysis was conducted using Student's unpaired *t* tests. In the following figures and tables, the statistical analysis was conducted between cells expressing the R424H mutant and those expressing GFP or between cells expressing R424H mutant and those expressing WT subunits. $^{**}P < 0.01$ and $^{***}P < 0.001$.

not affect the survival of granule cells. The difference in cell survival between PCs and granule cells may be because cultured granule cells do not express endogenous mKv3.3 protein (Supplemental Fig. S3*C*), and R424H mutant subunits were thus unable to form multimeric channels with the endogenous mKv3.3 subunits in the cells (see Discussion). These results indicate that R424H mutant subunits induced PC death and worsened their survival in a day-dependent manner.

To examine the cell death-induced morphological defects in the nuclei of PCs, cerebellar cultures expressing GFP alone, WT mKv3.3 or the R424H mutant were stained with Hoechst 33342 at DIV 8 (Fig. 2*F*). Chromatin in nuclei of GFP- or WT-expressing PCs was stained moderately, with some small bright granules (Fig. 2*F*, arrows in GFP and WT panels), demonstrating normal nuclear morphology. In contrast, PCs expressing R424H mutant subunits showed clear chromatin condensation (Fig. 2*F*, arrowhead in R424H panel). The percentages of PCs exhibiting this chromatin condensation were significantly different between R424H mutant-expressing PCs and the control group (Fig. 2*G*; $P < 0.001$ by Student's unpaired *t* test). These results suggest that the expression of R424H mutant subunits might induce apoptotic cell death in PCs.

At DIV 7, several neurites were observed in GFP- and WT-expressing PCs, which had morphologies similar to those of R424H mutant-expressing PCs at this stage (Fig. 3*Aa′*, *Ba′* and *Ca′*). However, at DIV 11, GFP- and WT-expressing PCs had elongated immature dendrites, whereas R424H mutant-expressing PCs did not show dendritic extension (Fig. 3*Ab′*, *Bb′* and *Cb′*). Sholl analyses of the dendritic arbors revealed that the number of dendritic intersections in R424H mutant-expressing PCs was significantly smaller than that in GFP-expressing (Fig. 3*D*, at distances of 10–50 μm from the cell body; $P < 0.01$) or WT-expressing PCs (Fig. 3*D*, at distances of 10–40 μm; $P < 0.01$). These results clearly demonstrate that in addition to the induction of cell death, expression of R424H mutant subunits in PCs decreases the survival rate and impairs dendritic development.

R424H mutant-expressing PCs exhibit lower outward current density

The results using *Xenopus* oocytes showed that expression of R424H mutant subunits significantly modulated WT mKv3.3 channel function (Fig. 1 and Supplemental Fig. S2). Thus, similar effects would be predicted in PCs lentivirally expressing R424H mutant subunits. In order to determine how these electrophysiological properties were affected, whole-cell patch-clamp recordings were performed using cultured PCs expressing GFP only, WT subunits or R424H mutant subunits at DIV 8–10.

Purkinje cells could be identified by their large cell bodies (cell body diameters of PCs at DIV 10, 17.2 ± 2.6 μm, $n = 78$; those of other neurons, 7.26 ± 1.7 μm, $n = 226$), and the recordings were confirmed by a combination of intracellular staining and immunocytochemical staining (Supplemental Fig. S4*A*). The cell capacitance of R424H mutant-expressing PCs was significantly lower than that of GFP- or WT-expressing PCs (Table 1; $P < 0.001$ in R424H *versus* GFP and in R424H *versus* WT), reflecting the impairment of dendritic development (Fig. 3*D*). However, the resting membrane potential and input resistance of R424H mutant-expressing PCs showed no difference when

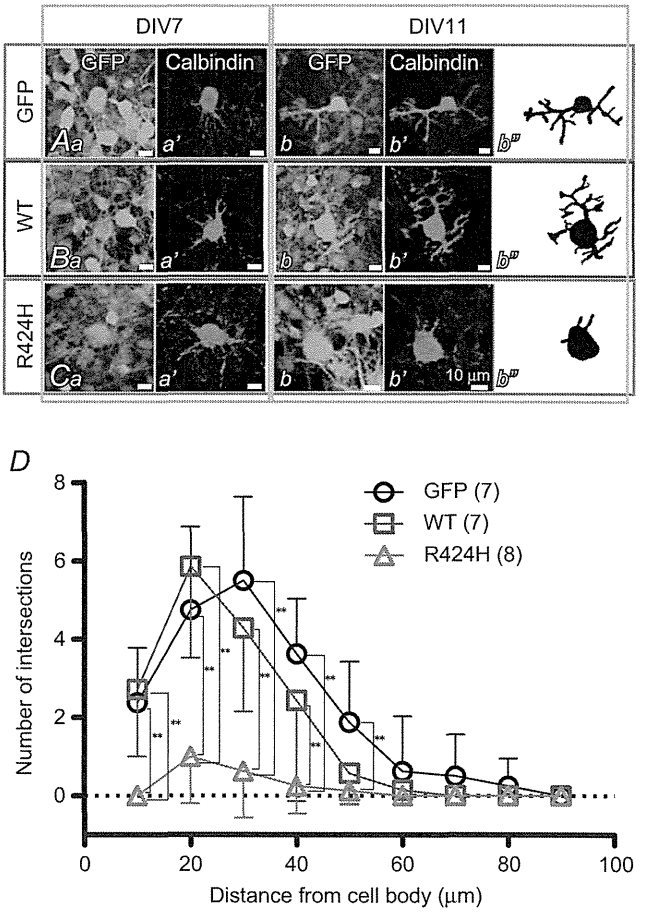

Figure 3. R424H mutant-expressing PCs exhibit impaired dendritic development
A–*C*, immunofluorescence images of PCs expressing GFP alone (*Aa*–*b′*), WT subunits and GFP (*Ba*–*b′*) and R424H mutant subunits and GFP (*Ca*–*b′*). *Ab″*, *Bb″* and *Cb″*, morphology of PCs expressing GFP (*Ab″*), WT subunits and GFP (*Bb″*) and R424H mutant subunits and GFP (*Cb″*) are depicted for clarity. Each PC was traced using Neurolucida software. *D*, summary of dendrite complexity measured by Sholl analysis. Concentric spheres were centred on the cell body, and the radii were incremented by 10 μm. The number of branching points within each sphere was plotted as dendrite complexity (i.e. the number of intersections). $^{**}P < 0.01$.